Gravitational Millilensing as a Probe of Dark Halo Substructure

Saghar Asadi

Supervisor:
Erik Zackrisson

Master of Science Thesis in Astronomy

Department of Astronomy

Stockholm University
May 2012

Abstract

During the last 80 years of studying dark matter, the cold dark matter model has succeeded to provide a coherent description of the universe at galactic and extragalactic scales. However, its subgalactic-scale predictions are plagued by a number of unsettled questions. One such issue is "the missing satellites problem". Along with the theoretical model, observational aspects of cosmology have also been substantially improved during the past century. The perspective of new radio arrays in the near future promises very high resolution observations in this field. Regarding gravitational lensing effects, obtaining sufficient observational data with submilliarcsecond angular resolution would shed light on such subgalactic challenges of the cold dark matter model. In this endeavour, performing simulations to imitate what the observational data of such telescopes would look like, provides us with a deeper insight on the type of sources and frequency bands in which we expect to detect the desired lensing effects.

In the present work, we run a series of simulations which examine the detectability of three different dark halo substructures with different VLBI observational modes.

Our results show that to detect lensing signatures made by standard dark halo substructures with current and foreseeing VLBI observational modes, we need to focus on large sources, such as radio-loud quasars which are manifested as ∼100-pc sized jets in certain frequency bands. However, if, as some astronomers propose, some fraction of the dark matter is in the form of intermediate-mass black holes with masses ranging from $\sim 10^3 M_\odot$ to $\sim 10^6 M_\odot$, these observations should be able to confirm it.

Contents

1 Introduction **2**

2 Gravitational Lensing **4**

2.1 Mathematical Description 5

2.2 Strong and Weak Lensing 8

2.2.1 Strong Lensing 9

2.2.2 Strong Lensing Regimes 10

2.2.3 Astrometric Perturbation 11

2.2.4 Time Delay 11

2.2.5 Flux Ratio Anomalies 12

3 Dark Halo Substructures **14**

3.1 The Cold Dark Matter Model 14

3.2 Halo Substructures in the CDM Model 15

3.2.1 SIS and NFW 17

3.3 Alternative Forms of DM Halo Substructures 17

3.3.1 Intermediate-Mass Black Holes 17

3.3.2 Ultracompact Minihalos 19

4 Compound Lensing Simulations **20**

4.1 The Host Halo 22

4.2 The Halo Substructure 23

4.3 The Lens Equation 24

5 Results **25**

5.1 Simulation Settings and Assumptions 26

5.1.1 Cosmology 26

5.1.2 Redshift Combination of the Lens System 27

5.1.3 Angular Resolution 28

5.1.4 Substructure Mass Function 28

5.1.5 Source Size 31

5.1.6 Dark Matter Mass Fraction 31

5.2 Statistical Approach (Random Subhalo Distribution) 32

5.2.1 IMBHs 32

5.2.2 UCMHs 32

5.2.3 NFWs 33

5.3 Deterministic Approach (Subhalo Cross Section) 34

5.4 Mathematical Analysis 38

5.5 Conclusions 40

5.5.1 Detecting IMBHs 40

5.5.2 Detecting UCMHs 41

5.5.3 Detecting NFWs 42

6 Discussion **49**

References **55**

CHAPTER 1

Introduction

THE first half of twentieth century witnessed major changes in cosmology. The first detection of dark matter by Zwicky (1933) gave rise to one of the most prominent mysteries in cosmology to this date. The fact that dark matter most significantly interacts through gravitational fields makes it relevant in the context of another cosmological phenomenon which came into use in the beginning of the previous century; *gravitational lensing*.

The complete development of general relativity made it possible to fully describe the long-known phenomenon of bending light when passing through a strong gravitational field. Along with the theory, improved observational facilities provided the possibility of making use of this phenomenon for objects beyond the local universe. On the other hand, the existence of a mysterious type of matter was broadly accepted and the search for the nature and properties of *dark matter* became a popular field of research in cosmology. Gravitational lensing, at many levels, seems to be an advantageous tool for dark matter hunters, since it applies to any object with a gravitational field, independent of the origin of their mass.

Dark matter properties have been studied for the last 80 years and even though the cold dark matter model has come up with successful predictions at galactic and extragalactic scales, its subgalactic-scale predictions are not convincing yet. The improvements in observational instruments have also shed light on subgalactic-scale cosmology. The perspective of new radio arrays, the Atacama Large Millimeter Array (ALMA) for instance, in the near future promises very-high-resolution observations in this field. Regarding gravitational lensing effects, subgalactic challenges of the cold dark matter model could be pushed toward their

solutions when sufficient observational data with submilliarcsecond angular resolution are obtained. Therefore, performing simulations to imitate what the observational data of such telescopes would look like, provides us with a better insight about the type of sources and frequency bands in which we expect to detect the desired lensing effects.

This work presents the results from a set of ray-tracing simulations of compound gravitational lensing effects by dark halo substructures of different types on radio-loud quasars at high redshifts. The simulation code rests upon the flat cold dark matter model and calculates the gravitational lensing effects on a given source due to the presence of a lensing galaxy and its substructures.

The following two chapters of this thesis consist of the theoretical background of the two main subjects of the problem; the gravitational lensing phenomenon (Chapter 2), and the dark halo substructures according to the cold dark matter model (Chapter 3). In chapter 4, we explain the computer simulation used throughout the work, and chapter 5 presents our results and the assumptions we have made to simulate real observational cases. Last, but not least, is the discussion (Chapter 6), in which we discuss the shortcomings of the present work and compare our results to the observational evidence at the current time.

CHAPTER 2

Gravitational Lensing

ALTHOUGH a hallmark of Einstein's general relativity (GR), the deflection of light is a predictable phenomenon based upon the Newtonian mechanics. In Newtonian description, light photons are treated as test particles being influenced by gravity of a massive object. Therefore, a test particle, passing with velocity v near a point-like massive object, M, with an impact parameter ξ, is deflected by an angle α. Considering a very small deflection angle (which is mostly the case in cosmology), α is given by

$$\alpha \simeq \frac{4GM}{v^2\xi}. \tag{2.1}$$

In the case of a light beam, where $v = c$, passing very close to the surface of the Sun, the deflection angle turns out to be $\sim 0.85''$. This value coincides with what was obtained by Einstein prior to the final formulation of GR, provided space is considered Euclidean not affected by gravity of the Sun. However, the pre-relativistic predicted deflection angle is half the predicted angle by general relativity in its fully developed form. The factor added by general relativity represents the local spatial curvature produced by the mass and was proven to be consistent with observational results in 1919 for the first time. Several Groups measured the angular shift of stars projected close to the limb of the Sun during a total eclipse Dyson et al. (1920). This served as the second evidence in support of GR, after perihelion precession of Mercury. Based on the calculation using the generalization of this phenomenon for two distant stars, it was generally accepted that the separated images of a star due to

the gravity of another star was impossible to detect with the technology of the day. A few years later, Fritz Zwicky suggested Zwicky (1937) that the effect of an extragalactic "nebula", i.e. a galaxy, rather than a foreground star is big enough and should have been observed by then. Even though his calculation was too optimistic due to the overestimate of the masses of galaxies at that time, the idea of utilizing this phenomenon as a "natural telescope" remained as a curiosity until 1979 when for the first time two identical quasars ($0957 + 561$ A & B) were revealed in an observation Walsh et al. (1979). The similarity of the spectra of the two quasars with the same redshifts, $z \sim 1.41$, and 6 arcseconds angular separation were mostly accepted to be convincing evidence for the fact that the two objects are physically associated. Furthermore, finding a galaxy at a lower redshift close to the two images lent more support to the idea that this was a gravitational lensing (GL) case.

Since then, several cases of gravitational lensing have been found and investigated. Therefore, this simple geometric phenomenon has become a widely-used tool in astronomy in recent decades. Observing lensed images of distant quasars or galaxies provides us with structural information of both the lens and the source such as their mass distributions.

GL has also opened up new windows to estimate some large-scale cosmological parameters such as the Hubble parameter. The idea is, as proposed by Refsdal (1964), to measure the time delay between the two images of a supernova; the farthest luminous objects of the time with intrinsic photometric variations. Since this time lag is related to the different paths of the light from the object, one can estimate H_0, with having an accurate model of the lensed source. It was about the time when the debate regarding the distance to the quasars came to an end. They were confirmed to be the most distant observed objects of the time. The distance estimate of quasars proposed even further intrinsically variable objects than supernovae to determine the Hubble's parameter using their gravitationally lensed images.

2.1 Mathematical Description

Various kinds of objects give rise to gravitational lensing; These objects can be point-like such as stars or extended lenses like galaxies and galaxy clusters. The commonly-assumed setup which produces GL effects is a point-like object (assuming an extended lens requires an integration over the projected lens area), lying on the connecting line between a point-like source and the observer. In this simplified case, light rays coming from the source are bent by the lens. Moreover, since in most cosmological cases the impact parameter of the lens is considerably small compared to the distances in the system, the lens is considered as a plane.

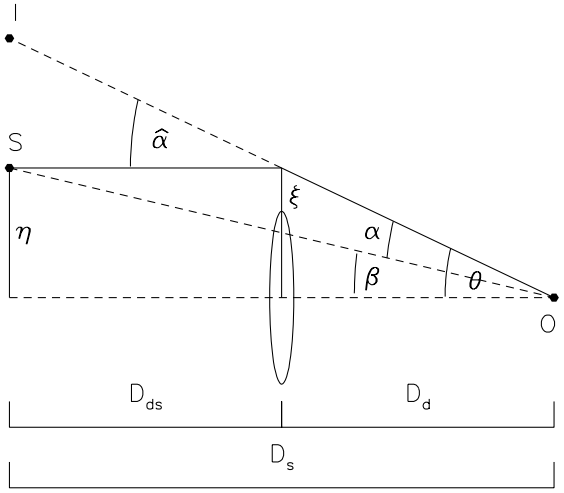

Figure 2.1: The relation between angles and distances in a GL setup as described by the lens equation. In this schematic figure, O represents the position of the observer, S is the source and the lens (deflector) is reduced to its projection on a plane perpendicular to the line of sight, as assumed in the "thin lens approximation". (Figure adopted from Narayan & Bartelmann (1996)).

This approximation is generally known as the "thin lens approximation".

The relation between the unlensed source position, $\boldsymbol{\beta}$, and the position of the image(s), $\boldsymbol{\theta}$, is called the *lens equation*. This equation can be derived geometrically from the setup displayed in figure 2.1 and symbolized mathematically as below:

$$\boldsymbol{\beta} = \boldsymbol{\theta} - \frac{D_{ds}}{D_s}\hat{\boldsymbol{\alpha}}(\boldsymbol{\xi}). \tag{2.2}$$

where the image position is $\boldsymbol{\theta} = \frac{\boldsymbol{\xi}}{D_d}$. Hence, by substituting α with the expression found in equation 2.1, we have

$$\boldsymbol{\beta} = \boldsymbol{\theta} - \frac{D_{ds}}{D_s D_d}\frac{4GM}{c^2\boldsymbol{\theta}}. \tag{2.3}$$

Alternatively, using the distance from the source to the optical axis, in the source plane, $\boldsymbol{\eta} = D_s\boldsymbol{\beta}$, the lens equation becomes

$$\boldsymbol{\eta} = \frac{D_s}{D_d}\boldsymbol{\xi} - D_{ds}\hat{\boldsymbol{\alpha}}(\boldsymbol{\xi}) \tag{2.4}$$

Given a certain mass distribution and a fixed $\boldsymbol{\xi}$, this equation can have more than one solutions for $\boldsymbol{\theta}$; each of which corresponds to an image of the source in the sky. Although obtaining the source position η from a given image position ξ using the lensing equation is straightforward, finding a general analytical solution for the position of the image(s) of a source at a given position is troublesome. Keeping in mind that the mapping of ξ to η is non-linear. There are, however, analytical models to solve this equation for simple matter distributions on the lens plane such as point-mass, axially symmetric, and elliptical lenses.

The deflection angle due to the surface mass density of the lens gives rise to a deflection potential ψ of the form $\boldsymbol{\alpha} = \nabla\psi$. Accordingly, another way of presenting the lensing equation is in the form of

$$\mathbf{y} = \nabla\left(\frac{1}{2}\mathbf{x}^2 - \psi(\mathbf{x})\right) \tag{2.5}$$

where $\mathbf{x} \equiv \frac{\boldsymbol{\xi}}{\xi_0}$ and $\mathbf{y} \equiv \frac{\boldsymbol{\eta}}{\eta_0}$ are dimensionless vectors, when ξ_0 and η_0 are length scales in the lens plane and the source plane, respectively. This form of expressing the lens equation leads to the formulation of Fermat's principle in GL theory such that

$$\nabla\phi(\mathbf{x}, \mathbf{y}) = 0 \tag{2.6}$$

where ϕ is a scalar function as below

$$\phi(\mathbf{x}, \mathbf{y}) = \frac{1}{2}(\mathbf{x} - \mathbf{y})^2 - \psi(\mathbf{x}) \tag{2.7}$$

Fermat's principle states that the light ray always chooses the path which takes the least time to pass through. Therefore, it can be used to relate the time delay between two separate images of a single source to the considered cosmology and mass distribution of the lens. Light deflection is a propagation phenomenon, thus just influences the shape of the light bundle from the source, and not the surface brightness. Therefore, for a monochromatic source, we have the received flux from the source as

$$S = I_\nu d\omega \tag{2.8}$$

where $d\omega$ is the differential solid angle, and I_ν is the monochromatic surface brightness. Since I_ν is not affected by gravitational deflection, the flux changes are merely mirrored in solid angle variation of the image. Hence, the *magnification* due to gravitational lensing is defined as the solid angle ratio of the observed image to that of the non-lensed source

$$|\mu| \equiv \frac{d\omega}{d\omega_0} \tag{2.9}$$

On the other hand, the solid angle is related to the angular position of the image (source), via the dimensionless quantities $\mathbf{x}$ ($\mathbf{y}$). Therefore, the magnification due to a circularly symmetric lens is given by

$$|\mu| = \frac{\theta d\theta}{\beta d\beta}. \tag{2.10}$$

One of the most interesting GL cases is the Einstein ring. The lensing setup which gives rise to a complete Einstein ring consists of a point-like source, with a spherically symmetric lens, both of which are collinear with the observer, i.e. the lens is centered around the line of sight between the observer and the source. Therefore, the observer sees a ring-shaped image with an angular radius of θ_E which is called the angular Einstein radius. This radius, θ_E is obtained by substituting $\beta = 0$ in equation 2.3 as:

$$\theta_E = \sqrt{\frac{4GM}{c^2}\frac{D_{LS}}{D_L D_S}}. \tag{2.11}$$

Where M represents the lens mass and D is the angular-diameter distances as in figure 2.1. Moreover, as it is immediately concluded from equation 2.10, for the *critical points* where $\beta = 0$, the magnification μ diverges. The "infinite" theoretical magnification points can be mapped into the source plane which gives a set of *caustic curves*. The number and relative positions of images of a single source change according to the position of the source with respect to such caustics in the source plane. (see figure 2.2).

2.2 Strong and Weak Lensing

The observable consequence of GL is usually known as magnified (or de-magnified) images of point sources, and distortions in the images of extended objects. The severity of the effect on the image depends on the alignment of the source, the lens and the observer. The closer the center of the lens to the line of sight between the observer and the source, the more significant the image distortion. Therefore, GL cases are categorized, according to the level of their magnifications, into two major regimes; *strong* and *weak* lensing. Strong lensing causes dramatic effects such as high magnifications, multiple images, luminous arcs and in some cases even complete Einstein rings. Although strong lensing is a rare effect, it is possible to be detected and studied individually for each case. Weak lensing, on the other hand, occurs when the center of the lens is further away from the observer's line of sight, i.e. $\theta > \theta_E$. Thus the images are weakly magnified or have small distortions. In contrast to strong lensing, weak lensing happens to be very common. Every line of sight is affected by weak lensing at some level hence this effect is detectable through statistical investigations of numerous objects.

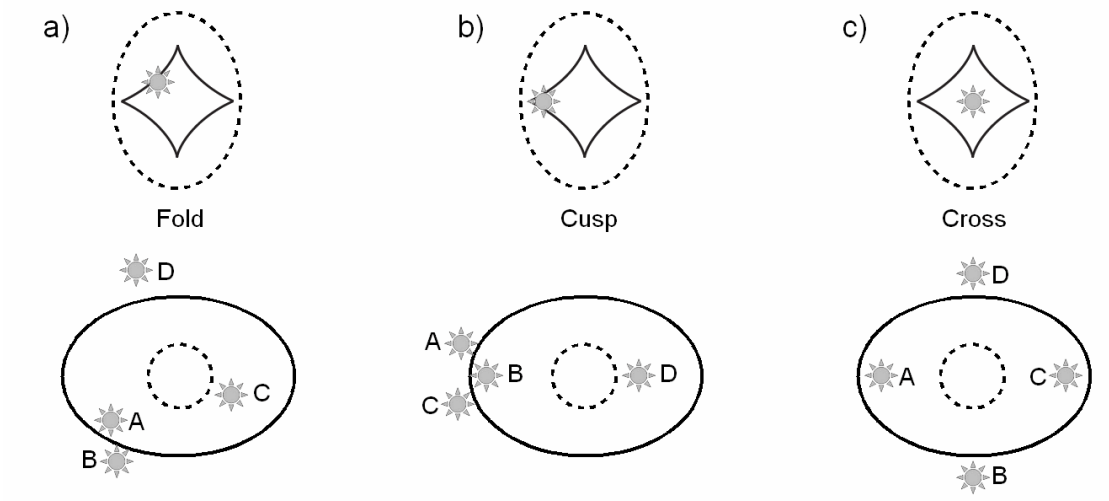

Figure 2.2: Different configurations of a four-image lens: a) Fold, b) Cusp and c) Cross. The upper row shows the caustics and position of the source (star) in the source plane. The solid line indicates the inner caustic and the dashed line the outer caustic. A source positioned inside the inner caustic produces five images. A source positioned between the inner and outer caustic produces three images, whereas a source positioned outside the outer caustic will not be multiply imaged. In the case of multiple images, one of the images is usually highly de-magnified, so that only four- and two-image lens systems are observed, respectively. The lower row shows the corresponding critical lines and resulting observable images in the lens plane. The inner caustic maps on the outer critical line and vice versa. A close pair (A, B) and a close triplet (A, B, C) are produced in the fold (a) and cusp (b) configurations, respectively. (Figure and caption adopted from Zackrisson & Riehm (2010))

2.2.1 Strong Lensing

As pointed out in the previous section, equation 2.3 can have multiple solutions. Moreover, when the "thin lens approximation" is valid, the surface mass density of the lens, i.e. the projected mass of the lens on the lens plane, determines the severity of the GL case. Accordingly, one can introduce the constant *critical surface mass density* Σ_{crit} such that for every θ in the lens equation 2.3, we have $\beta = 0$.

$$\Sigma_c = \frac{c^2}{4\pi G}\frac{D_{os}}{D_{ol}D_{ls}}. \tag{2.12}$$

In cases where $\Sigma > \Sigma_{\text{crit}}$, multiple images from the background source are produced. Exceeding the critical surface mass density may happen only for a part of a specific foreground

galaxy or galaxy cluster, the solid angle of which is then called the *strong lensing cross section.*

On the other hand, the magnification of the image due to the presence of the lens which was defined by equation 2.9, can also be expressed with the following relation

$$\mu = \frac{1}{(1-\kappa)^2 - |\vec{\gamma}|^2} \tag{2.13}$$

which is obtained by substituting the determinant of the Jacobian matrix for the lensing equation. In this form, there are two quantities upon which the magnification is dependent, *convergence* κ and *shear* vector $\vec{\gamma}$. Convergence, which describes the local isotropic magnification of the source, is a scalar quantity and is defined as the surface mass density of the lens in the unit of the critical surface density as below

$$\kappa \equiv \frac{\Sigma}{\Sigma_{\text{crit}}} \tag{2.14}$$

Shear is the measurement of the distortion of the source image and is quantified along each position component on the lens plane, thus a vector. The magnification for point sources is a tensor, only dependent on κ and $\vec{\gamma}$, however, for an extended source it is more complicated, depending on the internal surface brightness distribution of the source.

2.2.2 Strong Lensing Regimes

Strong lensing cases are studied within sub-regimes differing by the angular separation of multiple images produced by each.The angular separation of GL systems producing multiple images is typically of the order of the Einstein radius of the lens θ_E. Following is the terminology of giving names to various strong lensing separations.

Macrolensing refers to cases with typical angular separations, Einstein radii, of the order of *arcseconds.* Macrolensing can be thought as the combined effect of the dark and luminous matter of an isolated galaxy as well as the effect of galaxy clusters or multiple galaxies along the line of sight.

Millilensing (sometimes called *mesolensing*) effects, may be produced by satellite galaxies or their dark counterparts, dark matter subhalos, as well as small-scale objects such as intermediate-mass black holes (IMBHs), with typical multiple image separations in the order of *milliarcseconds.* Therefore, lensing effects in this regime potentially address one of the small-scale issues of the CDM theory, the so-called "missing satellites problem" which is mainly the subject of chapter 3. However, the compound effects due to this phenomenon

could be in a much larger regime, depending on the mass function and spatial distribution of these substructures Treu (2010).

Microlensing refers to Einstein radii of solar-mass lenses, i.e. the order of *microarcseconds*. Unlike macrolensing and millilensing, microlensing is a transient effect such that it is observable through monitoring a source for a period of time and recording its light curve. The apparent brightness of the source varies over time as the alignment of the lens system changes due to the moving lens. This type of GL is not considered in the present study.

Following the same convention, strong GL cases with smaller angular separations are referred to as nanolensing ($\theta_E \sim 10^{-9}$ arcseconds), picolensing ($\theta_E \sim 10^{-12}$ arcseconds), femtolensing ($\theta_E \sim 10^{-15}$ arcseconds), etc.

2.2.3 Astrometric Perturbation

The proximity of the projected image of a foreground massive object to a background source has a couple of effects. Among many, one is a change in the apparent position of the source. This effect which is usually accompanied by magnification or distortion effects is called the *astrometric effect*. Astrometric effects are therefore detectable mostly in dynamic cases, such as microlensing cases, where the observer can actually follow the differences in the relative positions in the system. One of these cases stems from the presence of substructures in the main lens such that where the deflector consists of a parent halo with a distribution of subhalos inside.

When it comes to the astrometric perturbation due to the substructure inside a subhalos, the image gets shifted from the original position of the macroimage, under the influence of a subhalo. Such effect is mostly sensitive to intermediate and high mass substructures Moustakas et al. (2009) and in clearly visible in the results of the present work (see figure 2.3). However, we are not interested in GL effects of this kind in our simulations.

2.2.4 Time Delay

Each image of a macrolensed source follows a different path to reach the observer, i.e. is subject to a different time delay. This time delay consists of two independent components; the geometrical and the gravitational component. The geometrical component springs from the fact that the path lengths are different for each image. The gravitational component, also known as the *Shapiro* effect, stems from the relativistic effect of retardation in strong gravitational fields. However, different time delays of various images cannot be observed if

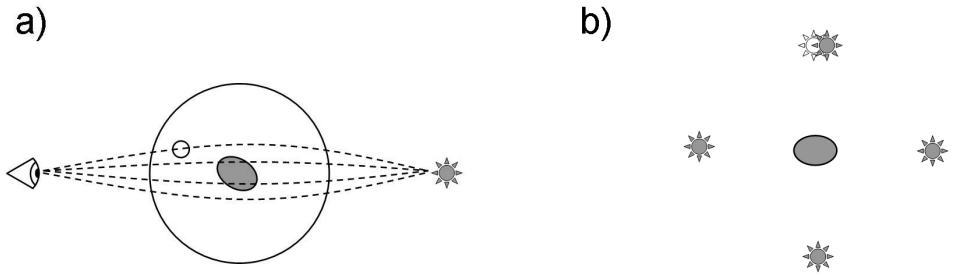

Figure 2.3: Astrometric perturbations. a) One of the multiple sightlines towards a distant light source passes through a dark subhalo. b) The images of the macro-lensed source are observed at the positions of the gray source symbols. Modeling of the lens system with a smooth lens potential predicts the position of the upper image at the white source symbol. The subhalo close to the sightline of the image causes a deflection on the order of a few tens of milliarcseconds. (Figure and caption adopted from Zackrisson & Riehm (2010))

the source is not intrinsically variable, since this effect is manifested in the phase difference of the light curves of various images. When it comes to subhalo hunting, the perturbation to the time delays between macroimages predicted by a smooth lens model serves as an evidence for the presence of substructures within the main lens (see figure 2.4). As Moustakas et al. (2009) argue, such an effect is only sensitive to subhalos at the high-mass end of the mass function.

Time delay is the only dimensional observable among GL observables reflecting the fact that it does change with the length scale of the lensing set-up. Given two lensing setups merely differing in angular-diameter distances, the only variable which breaks the degeneracy of the observables is time delays of various images.

2.2.5 Flux Ratio Anomalies

Gravitational lensing is a propagation phenomenon, thus it conserves the number of photons. On the other hand, the gravitational deflection influences the cross section of the light bundle differentially. Consequently, in order to conserve the flux, the area of the image(s) of the source changes. This leads to different magnifications for different macroimages, as explained in equation 2.9. However, mere determination of the flux of a single image does not provide any information due to the fact that the intrinsic flux of the source is unknown. The observable quantities turn out to be the flux ratio and positions of two separate macroimages of a single source which enable us to determine the properties of the lensing system in the

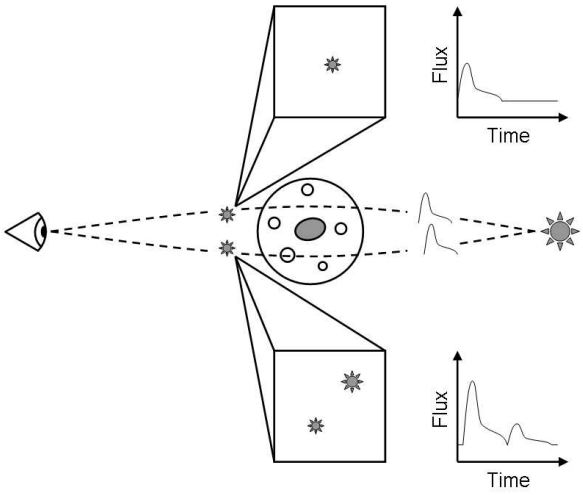

Figure 2.4: A galaxy with a dark matter halo produces distinct macroimages of a background light source. If this source dis- plays intrinsic variability, observable time delays between the different macroimages may occur. If one of the macroimages experiences further small-scale image splitting due to a sub- halo along the line of sight, a light echo may be observable in the affected macroimage. This may serve as a signature of millilensing in cases where the small-scale images blend into one due to insufficient angular resolution of the observations. (Figure and caption adopted from Zackrisson & Riehm (2010))

foreground. For instance, flux ratio anomalies of various macroimages of a single source, with respect to the simulations of the lens system with a smooth halo reveals the existence of substructures in galaxy-sized dark matter halos (see chapter 3).

CHAPTER 3

Dark Halo Substructures

3.1 The Cold Dark Matter Model

The Λ cold dark matter (ΛCDM) model is currently considered the standard model of cosmology. According to this model, $\sim 95\%$ of the universe is unaccounted for. The energy content of our universe at the current epoch is dominated ($\sim 72\%$) by a *cosmological constant*, Λ, the nature of which is still a matter of discussion. Moreover, $\sim 23\%$ of the energy density is in the form of *dark matter* which is made of "cold", "dark", and non-baryonic particles. These particles are called "dark", since they are only detectable through gravitational interactions and interact very weakly with photons and other standard-model particles. "Cold" refers to the fact that the velocities of dark matter particles were non-relativistic at the epoch of decoupling; and they are intrinsically different from the normal (baryonic) matter. The CDM model explains the anisotropies in cosmic microwave background (CMB) as observed by the Wilkinson microwave anisotropy probe (WMAP) in a more convincing way than the alternative forms of DM such as warm or hot DM (Spergel et al., 2007; Komatsu et al., 2009, 2011). Besides, the large-scale structure formation of the universe based upon the ΛCDM model is in agreement with most observational data. The subgalactic-scale predictions of the model, however, have not yet been confirmed observationally.

Two main challenges of the CDM model at subgalactic scales are:

1. **The predicted abundance of CDM halos is substantially larger than the observed galaxies of the corresponding mass range.**
   As pointed out in section 2.2.5, comparisons between the observed flux ratios of multiple images of a source show considerable discrepancies compared to the values expected from smooth dark halo models. This indicates the presence of substructures within dark matter halos which is also predicted by the CDM theory through the hierarchical dark structure formation in the universe (Metcalf & Zhao, 2002; Dalal & Kochanek, 2002; Keeton, 2001; Bradač et al., 2002). However, the observed flux ratio anomalies suggest more halo substructures than predicted by current CDM simulations. On the other hand, the simulated number of subhalos within a Milky-Way-sized dark matter halo exceeds the number of observed satellite galaxies in the vicinity of the Milky Way or Andromeda.

2. **Standard halos of the CDM model are too concentrated in the center compared to the observed halo parameters of dwarf galaxies.**
   While N-body simulations based upon the CDM theory predict a cuspy dark matter distribution of dark halos with a high central concentration, observations of the rotation curves of galaxies have failed to confirm this in their central regions.

This chapter serves as a more detailed introduction to the issues mentioned above and the role of gravitational lensing as an approach towards answering them. In section 3.2, we present the CDM model's galactic and subgalactic predictions and their discrepancies with observational data using standard density profiles for dark matter (sub)halos. Then, in section 3.3, we explain two alternative forms of substructures, which arise in alternative dark matter scenarios, and happen to be efficient millilenses.

3.2 Halo Substructures in the CDM Model

In the CDM model, dark matter distribution in the early universe is determined by quantum fluctuations when the universe was almost uniform. The amplitude of such fluctuations along with the model used for the secondary infall, constrains the lower mass limit of DM halos. Dark matter abundance of the universe has been redistributed merely under the influence of gravitational interactions since the formation of DM particles. Dark halos of different sizes form within a hierarchical process; smaller halos fall into the potential well of bigger

halos which swallow them through tidal stripping processes. With this mechanism, it may take several billion years for all small subunits to be completely dispersed into the smooth dark matter structure (White & Rees, 1978; Davis et al., 1985). Therefore, during this time, each halo consists of a smooth matter distribution which is contaminated by small-scale substructures. Simulations show that about 10% of a Milky-Way-sized dark matter halo, at the current epoch, is in substructures (Gao et al., 2011; Maciejewski et al., 2011). Furthermore, the hierarchical formation of larger halos, along with the given age of the universe (~ 13.7 Gyr) constraints the higher mass of DM halos to $\sim 10^{15} M_{\odot}$; since DM halos more massive than this limit did not have time to assemble yet.

On the other hand, the CDM scenario predicts that dwarf galaxies form in small dark halos, are expected to be observed within the CDM halos of large galaxies. High-resolution N-body simulations predict the number of dark matter satellites (with bounded masses $\gtrsim 10^8 M_{\odot}$ and tidally limited sizes $\gtrsim 1$ kpc) in the local group halo to be a few hundred, while observations have revealed satellite galaxies of the corresponding masses in the vicinity of the Milky Way and Andromeda to be less abundant by an order of magnitude (Moore et al., 1999; Klypin et al., 1999).

This discrepancy reflects one of the long-standing problems of the CDM model, referred to as the "missing satellites problem". Such a disagreement between the model and observational data is just one aspect of a more general problem: The discrepancy between the dwarf galaxy luminosity function and the low-mass end of the CDM halo mass function, i.e. the detected number of faint dwarf galaxies is significantly smaller than the predicted number of low-mass DM halos.

There are possible answers to this problem; some propose modifications to the CDM theory, in order to reduce the generated number of small-scale halos without affecting the large-scale structures, i.e. modifying the low-mass slope of DM halo mass function (Colombi et al., 1996; Bode et al., 2001; Spergel & Steinhardt, 2000). Other solutions suggest explanations for the lack of observed dwarf galaxies, by introducing "dark galaxies" or using astrophysical feedback processes which prevent star-formation in low-mass halos, i.e. explanations for the fain-end slope of the galaxy luminosity function (White & Rees, 1978; Kauffmann et al., 1993). Either way, GL induced by lenses in this mass range is one of the most promising means of solving the issue. The fact that GL is sensitive to massive objects, whether they are dark or luminous, may be able confirm or falsify the number density predictions of dark substructures by the CDM theory.

3.2.1 SIS and NFW

The most straightforward and commonly-used density profile for DM halos is the singular isothermal sphere (SIS) model. SIS halos are characterized by their velocity dispersion σ_V. In this model, the density decreases with increasing radius as

$$\rho_{\rm SIS}(r) = \frac{\sigma_V^2}{2\pi G r^2}, \tag{3.1}$$

where σ_V denotes the line-of-sight velocity dispersion and r represents the radial distance from the center.

Even though the SIS model is simple and commonly-used, neither theoretical arguments nor observational data support this model. However, strong lensing effects due to galaxy-sized lenses can be well described by this model. Therefore, SIS model is still used in galactic-scale lensing problems.

Predicted density profiles of isolated DM halos based on the CDM model are of the form $\rho(r) \propto r^{-\alpha}$ with the logarithmic slope $\alpha \approx 1$ in the central region and decreasing slope as r increases to $\alpha \approx 3$ for the outer regions around the virial radius (Navarro et al., 1996). This implies that these standard CDM halos (hereafter, called NFW for Navarro-Frenk-White) are expected to be significantly less concentrated in their central region than SIS halos with $\alpha = 2$. Along with their mass, NFW halos are described through a dimensionless concentration parameter $c \equiv R_{\rm vir}/R_s$. The mathematical representation of an NFW halo is

$$\rho_{\rm NFW}(r) = \frac{\rho_{\rm crit}\delta_c}{(r/R_s)(1 + r/R_s)^2}, \tag{3.2}$$

where $\rho_{\rm crit}$ represents the critical density of the universe ($\rho_{\rm crit} = \frac{3H^2}{8\pi G}$), δ_c is a dimensionless parameter linked to the concentration parameter c, and R_s is the scale radius corresponding to the radius at which the shape of the profile changes. Therefore, the density around the scale radius matches with the density described by the isothermal sphere.

3.3 Alternative Forms of DM Halo Substructures

3.3.1 Intermediate-Mass Black Holes

Intermediate-mass black holes IMBHs are expected to be remarkable gravitational lenses. However, these point-like masses are subject to strong observational constraints. Hence, there is not much evidence to support their existence.

IMBHs could form primordially or through the collapse of baryonic objects. Primordial black holes (PBHs) are believed to be formed through density fluctuations in the very early (typically $t << 1$ s) universe. Their masses can in principle range from the Planck mass, $10^{-5}g \simeq 10^{-35}M_{\odot}$, up to the most massive objects at the current universe (i.e. $\sim 10^{15}M_{\odot}$). Ricotti et al. (2008) present the upper mass limits on PBHs based on the effect that accretion onto these objects would have on the cosmic microwave background radiation and show that according to WMAP data the present abundance of PBHs with masses $\sim 10^{3}M_{\odot}$ and above is strongly limited. Hence, PBHs in this mass range are not expected to have a significant contribution to the dark matter at current epoch. (see figure 3.1). Moreover, the study by Carr et al. (2010) on PBHs with masses ranging from 10^{15} g to 10^{50} g confirms such strong limitations. However, there is a narrow mass range within which GL effects are weakly constrained that PBH detection via GL is promising (see section 5.1.4).

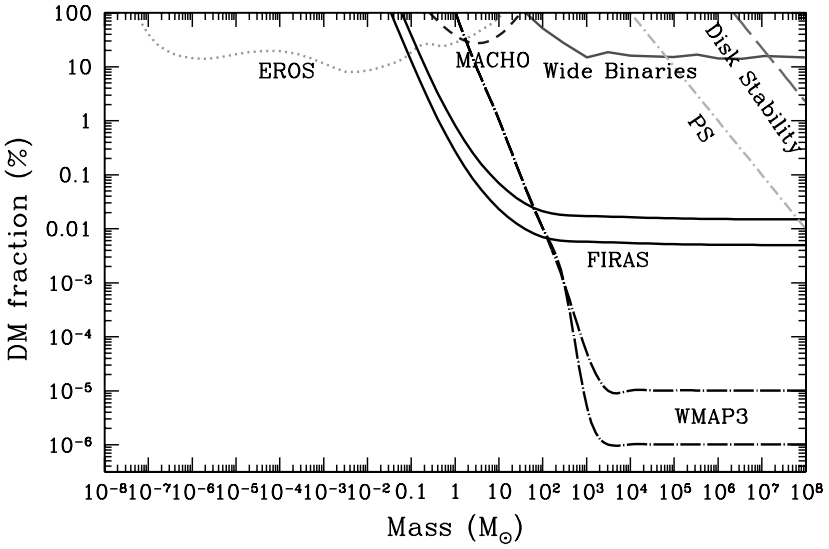

Figure 3.1: Upper limits on the present cosmological density of PBHs. *Thick* lines: observational constraints result from Ricotti et al. (2008). *Solid* lines: the upper limits using WMAP3 data (CMB anisotropies). *Dashed* lines: the limits using COBE FIRAS data (CMB spectral distortions). *Other* lines: previous upper limits from microlensing (EROS and MACHO collaborations) and dynamical constraints. (Figure adopted from Ricotti et al. (2008).)

An alternative formation scenario for IMBHs is through the collapse of baryonic matter. The mechanisms by which such IMBHs are formed is uncertain, however, it is clear that they are far more massive than the remnant black holes of normal population I or II stars. The suggested baryonic progenitors of such black holes are very massive population III stars (Maciejewski et al., 2011) or dense stellar clusters (Devecchi & Volonteri, 2009; Davies et al.,

2011). Moreover, a direct infall mechanism of the gas in the nuclei of protogalaxies is suggested by Begelman et al. (2006). Black holes formed through the latter mechanism initially have masses of $\sim 10M_{\odot}$ but can grow up to $\sim 10^4 - 10^6 M_{\odot}$.

3.3.2 Ultracompact Minihalos

Ultracompact minihalos (UCMHs) are primordial compact objects with SIS-like inner density profiles, $\rho_{\rm UCMH}(r) \propto r^{-2.25}$ providing us with good lensing signature prospects. Totani (2010) argues that the size evolution of early type galaxies from $z \approx 2$ to $z \approx 0$ can be explained only by non-baryonic dark compact objects of $\sim 10^5 M_{\odot}$.

The basic idea of the formation of UCMHs is the same as PBHs; through density fluctuations when the universe was less than $1s$ old. However, the fluctuations giving rise to UCMHs are supposed to be smaller in amplitude than those of PBHs by $2-4$ orders of magnitude which makes their existence more likely than that of PBHs Ricotti & Gould (2009). The density profile of UCMHs is estimated using simulations based on two scenarios for the formation of UCMHs; one is through density fluctuations, with amplitudes smaller than what gives rise to the collapse of PBHs, but big enough to leave a very compact object such as a UCMH. The second scenario describes a formation process of UCMHs over time such that UCMHs form through radial infall of a dark matter envelope onto a PBH. According to this process, the halo mass growth has been negligible during the epoch of radiation domination, while during the matter-dominated era they grew as $t^{2/3} \propto (1+z)^{-1}$ Ricotti & Gould (2009).

Furthermore, Scott & Sivertsson (2009) discuss the properties of UCMHs in self-annihilating WIMPs. If dark matter self annihilates, the central density of UCMHs is reduced. This makes them less efficient lenses (also uninteresting for our purpose), but at the same time hosts to other observable signatures such as gamma-ray emission. However, the Fermi gamma-ray space telescope has failed to detect the expected fluxes, so far (Buckley & Hooper, 2010; Hooper et al., 2007; Bringmann et al., 2012).

CHAPTER 4

Compound Lensing Simulations

THE ray-tracing fortran code to simulate compound gravitational lensing, *COMPLENS*, is based on the simulation used by Metcalf & Madau (2001) and written by *Jakob Jönsson* in 2002. This simulation, using CDM as the underlying cosmological model, is the means we use throughout this work to provide the desired lensing effects and test various cases produced by dark matter subhalos.

The three subroutines of this simulation are called *simsource*, *sisinfo*, and *complens*. *simsource* simulated the source, *sisinfo* generates the parent SIS halo, and the main part of the simulation is *complens* which adopts the substructures as input using a text file and solves the compound lens equation accordingly. The input parameters to each subroutine is outlined in table 4.1. We use *Complens* referring to the set of codes containing all three subroutines mentioned above.

The presumed model for the host halo is SIS with velocity dispersion of $\sigma_v = 240\ km/s$, corresponding to a mass $\sim 10^{13}\ M_\odot$ within the virial radius. The lens plane is assumed to be at redshift $z_l = 0.5$. Various models can be used to represent the substructures which are set by virtue of an input parameter. Among the available substructure models we investigate the following types; point-mass lenses for IMBHs, UCMHs, and NFWs. The substructures are by lying in the lens plane, thus sharing the redshift with the host halo. The arrangement of substructures is another input parameter to the simulation. We generate random positions based on the type of the substructure we are interested in, which is explained under the section related to each substructure model in chapter 5. *Complens* solves the lens equation to find

Table 4.1: **top left**: Input parameters used by *simsource* to describe the background source. **bottom left**: Input parameters passing to *sisinfo* and the purposes behind to adopt the SIS parent halo properties. **right**: *complens* input parameters and their interpretations, used to solve the lens equation.

simsource input	
L	Jet length (pc)
W	Jet width (pc)
ANG	Inclination angle (degree)

sisinfo input	
HOTSIG	Velocity dispersion (km/s)
HOSTY	Image location in source plane (pc)

complens input	
SUBFILE	Name of substructure file
GRIDN	Number of gridpoints
GRIDSIZE	Size of the grid (pc)
ZSOURCE	Source redshift
ZLENS	Lens redshift
SOL	Solution to lens equation
FSIGMA	Fraction of substructure

the position of all macroimages of the source produced by the SIS. The code then calculates the deflection angle due to substructures in the lens plane. The sources used in this report are radio jets at redshift $z_s = 2.0$. The final output of the simulation is an image of the source under the influence of the presence of both SIS host halo and dark substructures. Among many lensing effects in output images, we are only interested in small-scale morphological distortions in macroimages of the quasar. Although astrometric effects are also present in the output, we do not study them.

Complens simulates the lensing case making use of several free parameters. The free parameters of *Complens* describe the source, the smooth lens model and the lens substructures as below:

1. The source, size and shape of the projected image through three parameters of
   - Length, L, in pc
   - Width, W, in pc
   - Inclination angle, ANG, in $degree$s
2. The macrolens, i.e. the SIS parent halo
   - The linear velocity dispersion, σ_V, in km/s, accordingly the mass of the SIS halo.
   - The mass ratio of the dark matter in the form of substructure F_Σ

- The location of the image in the source plane, HOSTY, in *pc*

3. Dark substructures: Substructures are specified in an input text file which consists of the desired number of subclumps, each described by means of the following parameters.

   - density profile model (options: SIS, truncated SIS, point mass, NFW, truncated NFW, and UCMH)
   - position with respect to the macroimage in *pc*
   - concentration parameter, in the case of (truncated) NFW profiles
   - truncation radius, r_t in *pc* for truncated (SIS or NFW) profiles
   - mass

The internal resolution of the simulation is also a free parameter which is set through the GRIDSIZE input parameter in *pc* and the GRIDN parameter which sets the number of grids within the simulation region.

4.1 The Host Halo

The SIS halo is assumed to have the velocity dispersion and therefore the mass specified above. It also, without considering the substructures, has a smooth surface mass density which is calculated for each point on the lens plane.

As a consequence of the thin lens approximation (see chapter 2), the component of surface density due to the presence of the substructure in the lens adds up to the smooth surface density of the host halo. Therefore, the dark matter surface density within the simulation region, consists of these two components, is written as

$$\kappa_{\rm halo}(x) = \begin{cases} \kappa_{\rm smooth}(x) & \text{outside the simulation region} \\ [1 - F_{\Sigma}(x_0)]\,\kappa_{\rm smooth}(x) & \text{inside the simulation region} \end{cases} \tag{4.1}$$

Where F_{Σ} denotes the mass fraction of the dark matter halo in the form of substructures, and x_0 is the position of the substructure. This equation implies that the final observed magnification is the combined magnification owing to both macrolensing and millilensing effects. On the other hand, each simulation region is centered on the position of the macroimage in the absence of any substructures, therefore the astrometric shifts due to the presence of a subclump affect the position of the macroimage in the output frame.

The apparent shape and size of the lensed source in comparison to its intrinsic properties are described by the means of the *convergence* κ, and the *shear* γ. Convergence measures the absolute magnification of the source, i.e. size difference without variations in the shape, and shear is responsible for the ellipticity of the original source, such that for a primarily circular course, γ represents how much and in what direction the macroimage is elongated with respect to the original source image. In the case of an SIS, convergence and shear are equally influential, thus the total magnification due to the host halo is calculated as follows

$$\mu(\xi) = \frac{1}{(1-\kappa(\xi)^2)^2 - \gamma(\xi)^2} = \frac{1}{1-2\kappa(\xi)} \tag{4.2}$$

where ξ is the projected radial distance from the center of the halo on the lens plane and is a free parameter in *Complens*. In this work, the value of ξ is set such that the magnification of the macroimage corresponding to the first solution is ~ 10. This means that in all cases, the center of the region of the lens plane we are simulating is located at a distance of ~ 970pc from the center of the halo.

4.2 The Halo Substructure

Dark matter substructures within the parent halo are arranged by means of an input text file to *Complens*. The SUBFILE parameter is set to the name of the file including N lines each describing a substructure fixing the type, coordinates, mass, and complementary parameters differ for certain substructure type. The general template for each substructure type is following:

```
# SUBSTRUCT 0   <x>  <y>  <σ>
# SUBSTRUCT 1   <x>  <y>  <σ>  <r_t>
# SUBSTRUCT 2   <x>  <y>  <M>
# SUBSTRUCT 3   <x>  <y>  <c_200>  <M_200>
# SUBSTRUCT 4   <x>  <y>  <c_200>  <M_200>  <r_t>
# SUBSTRUCT 5   <x>  <y>  <M>
```

where the first integer sets the substructure type as indicating in table **??**, x and y are coordinate with respect to the center of the grid, i.e. the macroimage, M is the mass of the subclump. M_{200} and c_{200} represent the mass and concentration parameter of the substructures within the radius where the density of the dark matter is 200 times the mean

Table 4.2: The (sub)halo models covered in *Complens* and the integer numbers corresponding to each as identifiers in the input file to the code.

Subhalo model	identifier
SIS	0
Truncated SIS	1
Point mass	2
NFW	3
Truncated NFW	4
UCMH	5

density of the universe in the corresponding redshift. σ denotes the velocity dispersion which is used as a substitution of the mass for SIS models (SIS and truncated SIS), and r_t is the truncation radius assumed in the case of truncated NFW and truncated SIS subhalo models.

4.3 The Lens Equation

The lens equation within the simulation region is calculated assuming that the deflection angle of the image is the linear superposition of deflection angles caused by each possible subhalo present within the region (see equation 4.3). The amount of mass within each grid point of the simulation region is calculated using relation 4.1. Therefore, the deflection potential ψ is introduced for each gridpoint individually and the lens equation is solved independently.

$$\mathbf{y} = \mathbf{x} - \alpha_{\text{halo}}(\mathbf{x}) - \alpha_{\text{sub}}(\mathbf{x}). \tag{4.3}$$

Where the notations $\mathbf{x}$, $\mathbf{y}$ and α are the same as used in chapter 2. Accordingly, the lens equation is solved for each pixel of the grid and the lensed source image is produced.

CHAPTER 5

Results

OUR objective in this study is to investigate the sub-milliarcsecond scale lensing effects on a jet-like source, strongly lensed by a galaxy-sized dark matter halo, produced by the dark substructure within the main lens. We use the terms *subhalo* and *subclump* to denote the dark substructures located within a dark matter halo beside its smooth mass distribution. Through our simulations, we are interested in studying the cases where a background quasar is strongly lensed into multiple images and one or more subclumps happen to be projected sufficiently close to one of such macroimages to produce additional lensing effects.

Our results are obtained using two different approaches, the final results of which are consistent with each other, keeping in mind that we are interested in making order-of-magnitude estimates. The first approach involves doing statistics over numerous simulation runs for each subhalo type/mass, with random distribution of subhalos in the simulation region. This includes counting the detectably millilensed number of cases out of many runs as explained in section 5.2. The second approach follows a more deterministic method; the procedure consists of determining the cross section of each substructure of a certain type and mass and calculating the probability of detecting millilensing effects by means of analytical relations.

The final results are presented by means of two quantities; F_{Σ}^{PN} which predicts the "fraction" of projected dark matter mass in a given type/mass of subclump which provides millilensing effects in the presence of one subclump for every single multiply-imaged source; and P_{sim} which represents the probability of detecting sub-milliarcsecond-scale image distortions within a simulation region consisting of N subclumps. While P_{sim} is directly related to

the number of millilensed sources we expect to observe overall, F_{Σ}^{PN} provides us with a better understanding of the influence that the substructure model has on GL effects we are studying, independent of the abundance of each substructure type/mass with respect to others.

In the first section of the present chapter, section 5.1, we provide an overview of the simulation settings we used and the assumptions we made throughout the work. The second, 5.2, and third, 5.3, sections outline the two different methods of estimating F_{Σ}^{PN} and P_{sim} in more details. Section, 5.4, includes the mathematical framework leading us to extract the subhalo type/mass dependence of F_{Σ}^{PN} and P_{sim}. In the final, but most important section, 5.5, we present our results, i.e. the F_{Σ} as function of mass that different observations are able to probe.

5.1 Simulation Settings and Assumptions

Several parameters play role our simulation settings. Such parameters include the underlying cosmological model; the properties of the lens system; and the properties of telescopes with which we expect to test the results of this study. In this section, we skim through the parameters mentioned above with an emphasis on the most nontrivial ones, such as the dark matter substructures type/mass we studied and the dark matter mass fraction we assumed to be in such substructures.

Before going into details of simulation settings and assumptions, we need to make our definition of "detectability" clear. *Detectable* millilensing effects in the case of our study are classified into two main categories. Image splitting in at least one of the two macroimages; and image distortions, i.e. morphological perturbations of the macroimage of the source; with a scale larger than the corresponding resolution of the simulation in at least one of the solutions (see figure 5.1).

5.1.1 Cosmology

The underlying cosmological model of the present work is the flat Λ cold dark matter (ΛCDM) model. Therefore, throughout the study, the following cosmological parameters are used.

- Hubble parameter $h = H_0/(100\,\mathrm{kms}^{-1}\mathrm{Mpc}^{-1}) = 0.70$
- Matter density $\Omega_m = 0.27$
- Cosmological constant $\Omega_\Lambda = 0.73$

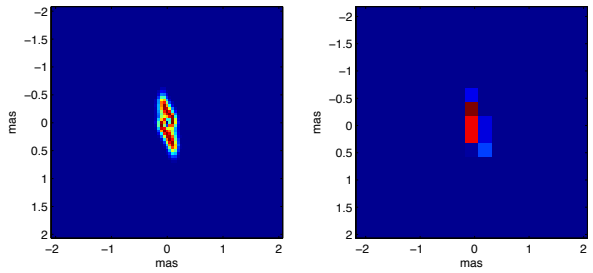

Figure 5.1: The detectability of GL effects in this work are examined by eye. Therefore, telling detectable and undetectable effects is not always straightforward, especially when it comes to image distortions in fainter parts of the image or in cases where the entire macroimage is covered only by a few pixels.

all in agreement with latest Wilkinson microwave anisotropy probe (WMAP) data (Spergel et al., 2007; Komatsu et al., 2009).

5.1.2 Redshift Combination of the Lens System

We assume radio-loud quasars at $z_s \sim 2.0$ as our sources. These quasars are strongly lensed into multiple images by dark-matter-dominated galaxies, with dark matter halos simulated by SIS models, at $z_l \sim 0.5$. As Yonehara et al. (2003) argue, this redshift combination provides a suitable lens system to detect CDM substructures. (see figure 5.2)

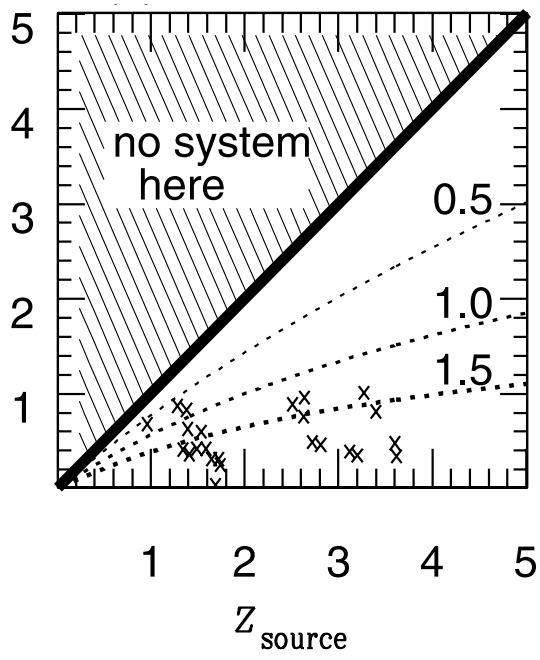

Figure 5.2: The source and lens redshift dependencies for SIS lenses of typical size θ_{SIS}. The dotted lines are contours for different values of $\theta_{SIS}(z_l, z_s)/\theta_{SIS}(z_l = 1, z_s = 2)$. As it is clear from the crosses on the diagram, redshift combination of $(z_l \sim 2.0, z_s \sim 0.5)$ is an acceptable canonical average combination of redshift-measured lens systems up to 2003. The upper left region is not taken into account since it is impossible to have lens systems with $z_l \leq z_s$ (Figure adopted from Yonehara et al. (2003)).

5.1.3 Angular Resolution

Present simulations have been designed to match the resolutions of present or upcoming observational arrays. The expected angular resolution of each array depends on its observing frequency. Therefore, we study our cases with three different pixel resolutions which are hereafter referred to as HR, LR and VLR (see below):

- $HR \approx 0.05\ mas$

  The highest resolution used in this work corresponds to a potential mode of observation connecting the full Atacama Large Millimeter Array (ALMA), including 50 antennae, to the global 3-mm array. These observations will be excecuted at 86 GHz with an angular resolution of $\sim 0.05mas$

- $LR \approx 0.25\ mas$

  The low resolution case simulates to the resolution obtained from observations with the European VLBI Network (EVN) at 22 GHz with angular resolution of $\sim 0.25mas$.

- $VLR \approx 0.7\ mas$

  The resolution available from observations with the global array, including the European VLBI Network (EVN) and the Very Long Baseline Array (VLBA), at 8.4 GHz corresponds the lowest resolution among our resolutions.

5.1.4 Substructure Mass Function

The mass range used for each subhalo model is constrained, either by observational detectability or theoretical constraints according to the literature. Whereas the lower limit is set by the detectability of millilensing effects in simulation outputs, the higher mass constraints are applied theoretically, except in NFW case which is elaborated on in section 5.1.4. As a result of the limitations mentioned above, the IMBH mass range does not overlap with either that of UCMHs or NFWs. On the contrary, UCMHs and NFWs overlap in the range $10^7 - 10^9 M_\odot$. Moreover, since we are only interested in making order-of-magnitude estimates, the smallest unit of subclump mass we are dealing with, during the entire work, is a decade in solar mass, i.e. $10M_\odot$. Therefore, all mass ranges are presented in $10M_\odot$ mass bins.

IMBHs

An elaborate work by Carr et al. (2010) points out different existing constraints on the dark matter fraction of PBHs within a wide mass range of $\sim 10^{-18} - 10^{17} M_{\odot}$. According to this work, the results of which are shown in figure 5.3, GL effects produced by such objects are less constrained in a narrow mass range between 10^2 to $10^4 M_{\odot}$.

On the other hand, Totani (2010) suggests that the size-evolution of early-type galaxies could be explained by assuming all non-baryonic cold dark matter in the form of dark compact objects with masses $\sim 10^5 M_{\odot}$. Accordingly, we assume IMBHs to have masses in the range of $10^2 - 10^6 M_{\odot}$. However, since $10^2 M_{\odot}$ IMBHs do not show millilensing effects in any of our simulated cases, we exclude them from all plots and calculations.

For simplicity, we do not consider a mass spectrum for IMBHs in present simulations. Therefore, we run four different sets of simulations each using IMBHs in a certain mass bin from 10^3 to $10^6 M_{\odot}$.

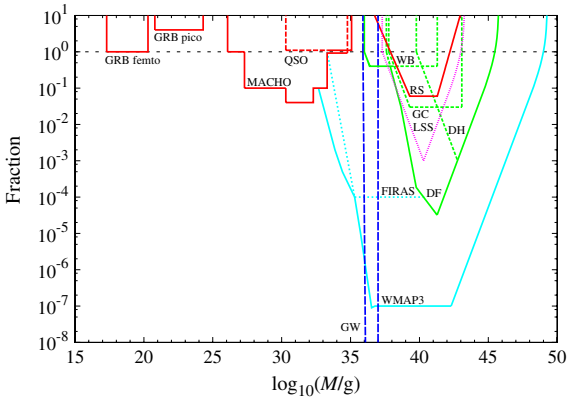

Figure 5.3: Overview of existing constraints on the dark matter fraction of PBHs at different masses.The mass range which is less constrained for lensing effects (Figure adopted from Carr et al. (2010)).

UCMHs

As pointed out previously in chapter 3, it is generally accepted that if dark matter is in the form of self-annihilating WIMPs, the central density of UCMHs is decreasing over time (Scott & Sivertsson, 2009) which makes them such inefficient lenses which are not expected to cause any detectable millilensing effects. However, if we envision UCMHs produced by non-annihilating dark matter candidates, they can be described by a density profile somewhat steeper than the singular isothermal sphere which keeps them in the contest to give rise to gravitational millilensing effects (Ricotti & Gould, 2009; Bringmann et al., 2011).

Similar to the case of IMBHs, for each UCMH mass bin a separate simulation is performed to study the GL effects produced by UCMHs in that mass bin individually. The adopted mass range for these subhalos is $10^6 - 10^{10} M_{\odot}$ which is constrained mostly due to detectability

limitations in sub-milliarcsecond scales from both sides.

NFWs

NFWs are assumed to have masses between $10^5 - 10^{10} M_\odot$. However, at some point we had to discard $10^{10} M_\odot$ subhalos. This is explained more in section 5.2.3.

Unlike IMBHs and UCMHs, the subhalo mass function adopted in the case of NFWs is of the form $\frac{dN}{dM} \propto M^{-\alpha}$, where $\alpha = 1.9$ (Springel et al. (2008), the Aquarius N-body simulation). Moreover, regarding NFW profiles, the *concentration parameter* c is also to set beside the mass of the subhalo which accordingly sets the scale radius, R_S, of the subhalo (recall that $c = R_{vir}/R_S$). The concentration parameters we adopt are from Zackrisson et al. (2008), which is the same as what is obtained by Macciò et al. (2008) with taking the redshift evolution of CDM density profiles, as derived by Bullock et al. (2001), into account; $c \propto (1+z_l)^{-1}$. This results in higher concentration parameters for subhalos with lower masses and is formulated as below

$$c = \frac{9}{1+z_l} \left(\frac{M_{vir}}{1.5 \times 10^{13} h^{-1} M_\odot} \right)^{-0.13} \tag{5.1}$$

In order to adopt the desired mass function, we performed a Monte Carlo (MC) sampling to generate an ensemble of subhalos in the mass range $10^5 - 10^{10} M_\odot$, divided into decades in solar mass and kept producing subhalos until the adopted $F_{\rm NFW}$ was fulfilled (see figure 5.4).

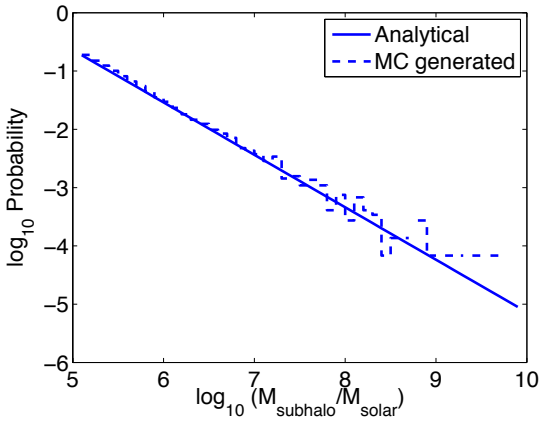

Figure 5.4: MC sampling of NFW subhalos to fulfill the desired $F_{\rm NFW} = 0.02$.

As it is seen in figure 5.4, the probability of MC-generated subclumps with higher masses deviates considerably from the analytical value, due to the fact that such massive subhalos include a substantial fraction of the total mass in substructures. However, such deviations do not make a big difference in our final results due to two main reasons.

1. The total mass of the NFWs consisting of the entire mass spectrum within our simulation region always remains very close to $10^{10} M_{\odot}$.

2. Since we generate numerous ensembles of subhalos randomly, this discrepancy is not biased towards higher or lower probabilities, overall.

5.1.5 Source Size

When it comes to the radio regime, quasars frequently manifest themselves as jets with sizes varying from ∼pc to ∼kpc, depends on the frequency band they are observed in (Torniainen et al., 2008). We assume *pc*-sized jets ($L = 4$ pc, $W = 1$ pc) in out HR and LR cases which is three orders of magnitude smaller than what Riehm et al. (2009) use. However, the source size we assume in the case of VLR lies in the order of ~ 100 pc due to the different frequency band we expect to do such observations in.

5.1.6 Dark Matter Mass Fraction

IMBHs

The fraction of dark matter mass, potentially in the form of IMBHs, is chosen to be the free parameter in our statistical approach explained in section 5.2. We repeat the simulation, increasing the dark matter mass fraction in IMBHs, F_{IMBH}, up to the point where the possibility of detecting millilensing effects in a simulation region with a number of subhalos of a given mass is sufficiently close to unity. Since the number density of subhalos of a given mass depends on F_{IMBH}, the number of subhalos within the simulation region changes with F_{IMBH} based upon equation 5.2.

UCMHs

As it is expected from their density profiles and mentioned in chapter 3, UCMHs are not as efficient lenses as IMBHs. Therefore, increasing F_{UCMH} in order to result in close to 100% millilensing detectability occurs for $F_{\mathrm{UCMH}} > 1$. Consequently, we keep $F_{\mathrm{UCMH}} = 1$ as a fixed parameter through all cases with UCMHs.

NFWs

N-body simulations suggest that the surface mass fraction of the dark matter in the form of subhalos in the mass range of NFW profiles is $\sim 0.2\%$ (Xu et al., 2010). However, the fraction

obtained from various lensing techniques such as flux ratio anomalies and perturbations of Einstein rings is larger by an order of magnitude (Chen et al., 2011). We treat simulations with NFWs separately for $F_{\rm NFW} = 0.02$ and $F_{\rm NFW} = 0.002$. However, as it is shown and explained in chapter 6, the NFW subhalos are so inefficient lenses that even in the most optimistic case of $F_{\rm NFW} = 0.02$, the probability of detecting millilensing effects due to such subhalos is negligibly small.

5.2 Statistical Approach (Random Subhalo Distribution)

5.2.1 IMBHs

The number density of substructures clustering within a parent halo depends on their relative contribution to the dark matter within that halo, as well as the masses of individual subhalos involved. As mentioned in section 5.1.6, we treat dark matter substructures consisting only of IMBHs such that $F_{\rm IMBH}$ is the free parameter of the simulation. Therefore, we adopt the dark matter fraction assumed to be in IMBHs within a certain mass bin. Besides, by applying the relation below, we calculate the associated number density of such subclumps.

$$n_{\rm sub} = \left(\frac{\Omega_{\rm sub}}{\Omega_{\rm CDM}}\right) \Sigma_{\rm CDM} \frac{1}{M_{\rm sub}} \tag{5.2}$$

Where $\frac{\Omega_{\rm sub}}{\Omega_{\rm CDM}} \equiv F_\Sigma$ is the dark matter fraction in the form of substructures, n_{milli} denotes the number density of millilenses, and $\Sigma_{\rm CDM}$ represents the surface mass density in cold dark matter in the lens plane, at the position of the macroimage simulated. This relation is applicable to all dark matter substructures independent of the density profile assumed for them, as along as the surface mass density of the lens is dominated by CDM, i.e. $\Sigma_{\rm CDM} \approx \Sigma_{\rm total}$.

Recalling from section 5.1.6, what we are interested in, regarding point-mass millilenses, is the smallest subhalo mass fraction $F_{\rm IMBH}$, sufficient for detectable millilensing effects to be present in essentially all macroimages. Therefore, as we increase the masses of individual IMBHs and keep $P_{\rm sim}^{N_{\rm IMBH}} \approx 1$, we determine $F_{\rm IMBH}^{P1}$ directly from statistical counting of simulation outputs.

5.2.2 UCMHs

UCMHs are expected to have shallower density profiles than IMBHs. Thus they are less efficient lenses and as pointed out in section 5.1.4, their detectable mass range starts from

$10^6 M_\odot$. On the other hand, for a given F_Σ the more massive the subhalo, the smaller its number density (see equation 5.2). Therefore, we need to use much larger simulation regions to fit a single UCMH in a simulation area as large as the region used for IMBHs. Enlarging the simulation region is computationally demanding. Besides, as the area of the simulation region increases, the fraction of the region covered by the macroimage decreases. The detectability of morphological effects in this study is examined by comparing (by eye) the millilensed macroimage with the original macroimage. Therefore, the macroimage size is required to be kept big enough, compared to the entire simulation area, such that the uncertainty of detectability in examining morphological changes by eye is not substantially larger than the angular resolution of the simulation. Such limitations lead us to use a different free parameter than the CDM mass fraction, to simulate UCMHs. We fix the values of $F_{\rm UCMH}$ and $N_{\rm UCMH}$ to one and determine the probability of detecting millilensing effects in an ensemble of simulations.

Looking at equation 5.2, for given values of $F_{\rm UCMH}$, $M_{\rm UCMH}$ and $N_{\rm UCMH}$, the smooth CDM mass density Σ_{CDM} within the simulation region is fixed. We need to keep in mind that equation 5.2 does not account for the increase in the surface density due to substructures. However, since the simulation region is much smaller than the entire projected surface area of the host halo, this assumption gives rise to slightly optimistic results of the detectability of UCMHs.

5.2.3 NFWs

For the two different cases of $F_{\rm NFW} = 0.02$ and $F_{\rm NFW} = 0.002$, we calculate the probability of observing millilensing effects, according to the mass distribution function of such subhalos in a specific simulation region. The sampling region is chosen considering the fact that the minimum required mass of the subclumps contained in the region is a few times $10^{10} M_\odot$ (otherwise, we cannot sample the entire mass range presented in section 5.1.4). A MC sampling is followed to generate various random subhalo distributions which fulfill the mass function $\frac{dN}{dM} \propto M^{-1.9}$, in the mass range $10^5 - 10^{10} M_\odot$, as explained in sections 5.1.4 & 5.1.6.

$M = 10^5 - 10^6 M_\odot$

Different NFW masses were checked for their millilensing effects. Test runs were made with single subhalos in $10 M_\odot$ bins. NFWs with masses 10^5 and 10^6 solar masses proved to be completely inefficient lenses at this mass scale. Even with very small impact parameters, no

GL effect due to these subhalos was detectable in the millilensing regime.

$M = 10^7 - 10^9 M_\odot$

According to our test runs, NFWs in the mass range $10^7 - 10^9 M_\odot$ are expected to show image distortions or image separations, detectable in our HR and LR simulations. On the other hand, simulated observations with VLR miss all kinds of millilensing effects due to $10^7 M_\odot$ NFWs, whereas such effects are still detectable for $10^8 - 10^9 M_\odot$ subclumps.

$M = 10^{10} M_\odot$

Taking the NFW concentration parameter c into consideration, the more massive the subhalo, the smaller is the corresponding concentration parameter, i.e. NFWs with lower mass are more centrally concentrated that the more massive ones. Recalling from section 5.1.4, $c = R_{\text{vir}}/R_S$. Therefore, decreasing c represents an increase in R_S faster than in R_{vir}. On the other hand, in our case of study, the dark matter mass density influencing the source image is a combination of that of the macrolens, i.e. the SIS parent halo, and a NFW subhalo. In other words, we are not dealing with isolated halos, the case we are studying is a subhalo within a bigger halo.

Moreover, the NFW density profile for $R < R_S$ is significantly shallower than the isothermal density profile. Therefore, the isothermal density profile of the macrolens dominates in this region. Such effect would not be detected in our simulations up to the case of $M_{\text{NFW}} \approx 10^{10} M_\odot$ where the scale radius R_S is large enough to be seen such as a smooth isothermal density profile. This phenomenon makes looking at subhalos as massive as $10^{10} M_\odot$ different than the less massive ones. Although, it is possible to see "regular" millilensing effects due to these subhalos with impact parameters larger than the scale radius, R_S seems to be larger than the simulation region we are able to probe in our simulations. Moreover, since the probability of finding subhalos as massive as $10^{10} M_\odot$ sufficiently close to a macroimage is as small as $\sim 10^{-5}$, we exclude them from the test.

5.3 Deterministic Approach (Subhalo Cross Section)

Different models and masses of dark matter subhalos influence the macroimage differently. We describe such variation by means of the *effective cross section* of each subhalo. This quantity represents an area around the subhalo within which the macroimage is subject to

a substantial shear/convergence due to the subhalo. The cross section is influenced by both the physics of the subclump and the our numerical resolution.

The resolution-dependency is caused by the limitation of the size of the gridpoint; If the length-scale of the image distortion/separation caused by a millilens is smaller or on the order of the gridpoint size, lensing and gridding effects are indistinguishable. The inaccuracy stems from smoothing the radio beam with a Gaussian profile of the required resolution. The cross section value also depends on the size of the macroimage. Such technical shortcomings make the estimate of the cross section less accurate in the case of less efficient, i.e. less massive or with shallower density profile, millilenses since they have smaller mass densities, thus smaller Einstein radii, which give rise to the same gridding issue. This is especially crucial in the case of the smaller jet since the entire jet is covered by just a few pixels.

The physical subclump type-dependency is such that generally, subhalos with steeper density profiles have larger cross sections, i.e. are more efficient lenses. Moreover, for a given subhalo type, the cross section increases with increasing mass. The estimated cross sections for all cases explored in this study are shown in figure 5.5 and listed in tables 5.1, 5.2, and 5.3. The procedure of determining the cross sections is such that for a given source size

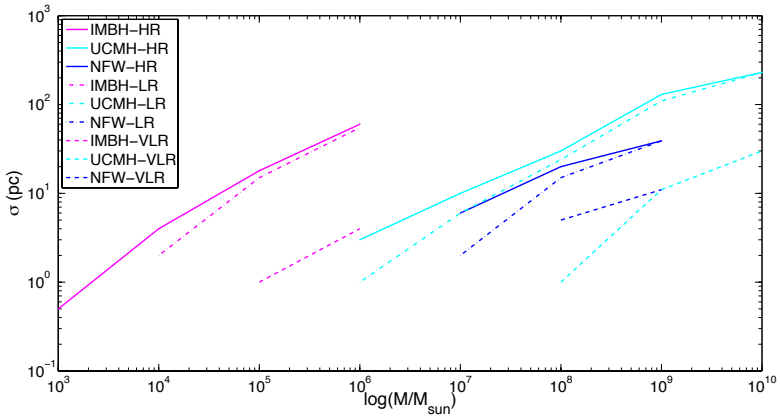

Figure 5.5: Final cross sections obtained for different substructure types/masses corresponding to various telescopes. *Magenta* lines denote IMBHs, the *cyan*s correspond to UCMHs and *blue* lines are representing NFWs. For each substructure type, the cross sections obtained in HR, LR and VLR cases are shown with *solid*, *dashed-dotted* and *dashed* lines, respectively. Note that all HR and LR values converge at higher masses, since the effects due to more massive halos provide better detectability. Whereas, VLR trends lie far from the corresponding HR and LR ones which is due to the jet size-difference observed by their different frequency bands.

Table 5.1: Final cross section values determined for various IMBH masses.

Frequency (GHz)	Mass ($M_\odot$)	σ (pc)
86	10^3	0.5
86	10^4	4
86	10^5	18
86	10^6	60
22	10^4	2
22	10^5	15
22	10^6	55
8.4	10^5	12
8.4	10^6	40

Table 5.2: Final cross section values determined for various UCMH masses.

Frequency (GHz)	Mass ($M_\odot$)	σ (pc)
86	10^6	3
86	10^7	10
86	10^8	30
86	10^9	130
86	10^{10}	230
22	10^6	1
22	10^7	6
22	10^8	24
22	10^9	110
22	10^{10}	230
8.4	10^8	14
8.4	10^9	115
8.4	10^{10}	300

and resolution, we move the subhalo along two perpendicular axes using 1-, 2-, 5-, or 10-pc steps. During this process, two values are obtained as the largest effective impact parameters between the macroimage and the projected position of the millilens.

A test for the determination of detectability of the effect was to check whether the difference between the obtained values along and across the radio source are consistent with the macroimage size, i.e. the magnified jet length (see figure 5.6). All values showed an acceptable consistency in this regard which supports the validity of our method.

Frequency (GHz)	Mass ($M_\odot$)	σ (pc)
86	10^7	6
86	10^8	20
86	10^9	39
22	10^7	2
22	10^8	15
22	10^9	39
8.4	10^8	50
8.4	10^9	110

Table 5.3: Final cross section values determined for various NFW masses.

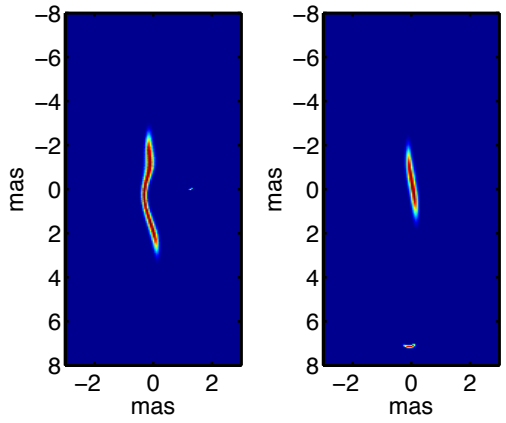

Figure 5.6: The cross section is a quantity related to the Einstein radius of the substructure. Therefore, a possible way to examine the viability of our results in determining the cross section is to check if the difference in the effective distance obtained along a certain source due to a certain substructure and the effective distance across the source macroimage is approximately equal to the jet length. The two images above show the effective distances along and across a small source (jet size 4 pc) produced by a an IMBH of $M_{\mathrm{IMBH}} = 10^5 M_\odot$. The positions of the IMBHs are indicated by white dots.

Now that the corresponding cross section to each subhalo is determined, we have to estimate the probability of having detectable millilensing effects due to each subhalo type and mass bin. The validity of this estimation can be examined by comparing the results with the output statistics of numerous random sample runs with *Complens*. However, this comparison has to be done by making use of a translation between two sets of outputs through the mathematical framework explained in section 5.4. The ultimate values we can compare are the probability of having millilensing effects detectable for a given set of input parameters,

$P^N_{\rm sim}$, and the dark matter mass ratio required to have all observed/simulated cases affected by detectable millilensing effects due to subhalos, F^{P1}_{Σ}. The details of these calculations is the subject of section 5.4

5.4 Mathematical Analysis

As pointed out in the beginning of this chapter, the two parameters we are interested in presenting our results through are not directly available from our simulation outputs. Therefore, some mathematical analysis is needed to calculate the desired parameters, $F^{\rm PN}_{\Sigma}$ and $P_{\rm sim}$, for millilenses of different types and masses. In the present section, we first introduce the mathematical notation, the sub/superscripts we use to set the conditions under which the parameter is calculated; and then present mathematical relations to derive $P_{\rm sim}$ and $F^{\rm PN}_{\Sigma}$.

To follow the relations in this section, we need to clarify our mathematical notations first. The general format of all parameters is X^Z_Y where,

- "X" is the parameter we are talking about, the main parameters and the quantity each represents are shown in table 5.4.

Table 5.4: The main input/output parameters involved in the mathematical analysis.

"X" Symbol	meaning	input or output
F_Σ	CDM mass fraction	UCMH/NFW: input
	in millilenses	IMBH: output
A	surface area	input
N	number of substructures	input
P	millilensing detection probability	output

- "Y" denotes whether the parameter "X" is used for the simulation, *sim*, or the Monte Carlo sampling, *MC* (see table 5.5).

- "Z" represents the condition under which "X" is set or calculated. The three different conditions with their corresponding notations are outlined in table 5.6.

Following are general relations which hold independent of the substructure model and the corresponding constraints we use in collecting simulation results.

Using equation 5.2, for fixed F_Σ and A, we have the proportionality below for each $M_{\rm sub}$

Table 5.5: The two subscripts which show whether the main parameter relates to the Monte Carlo sampling or the simulation run. When no subscript is used, the relation can be used generally for both cases.

"Y" Symbol	meaning
sim	adopted in/calculated for the simulation
MC	adopted in/calculated for the Monte Carlo sampling

Table 5.6: The conditions set to each simulation run is shown as a superscript on each describing parameter. These assumptions help running each simulation as computationally efficient as possible beside being able to translate the achieved results to more general conditions.

"Z" Symbol	meaning
N	$N = 1$
P	$P \approx 1$
F_Σ	$F_\Sigma \approx 1$

$$N \propto \frac{1}{M_{\rm sub}} \tag{5.3}$$

Besides, one would naively expect that increasing the number density of millilenses increases the probability of detecting millilensing effects. Therefore,

$$P \propto N/A \tag{5.4}$$

This implies that if we want to calculate what the probability would be if there is only one substructure in a given area, we find

$$P^N \approx \frac{P}{N} \tag{5.5}$$

On the other hand, considering 5.2 and 5.5, for fixed sampling and simulation regions, i.e. $A_{\rm MC}$ and $A_{\rm sim}$, we know that

$$F_\Sigma \propto P \tag{5.6}$$

$$\Rightarrow \frac{F_{\Sigma\,\rm sim}}{P_{\rm sim}} = \frac{F_\Sigma^{\rm PN}}{P_{\rm sim} \approx 1}. \tag{5.7}$$

Therefore, both desired parameters P and F_{Σ}^{P} are calculated for each substructure using the data collected from the corresponding simulations runs, independently for each approach, as shown in table 5.7.

Table 5.7: The mathematical relations through which the final results are obtained using the simulation results from the two approaches.

Approach	P_{sim}	F_{Σ}^{PN}
Statistical	direct count	$\frac{F_{\Sigma}}{P_{\mathrm{sim}}}$
Deterministic (cross-section)	$\frac{N_{\mathrm{sim}}/A_{\mathrm{sim}}}{A_{\mathrm{affected}}}$	$\frac{F_{\Sigma}}{P_{\mathrm{sim}}}$

Beside the parameters introduced earlier in table 5.4, there is a new surface are used in table 5.7, A_{affected}. A_{affected} is the area around each macroimage which is influenced by millilenses considering the cross-section values listed in tables 5.1 to 5.3. The fact that the macroimage is a jet, rather than a point-like or a circular source, makes the affected area dependent on the macroimage size as well as the cross section value.

5.5 Conclusions

5.5.1 Detecting IMBHs

The probability of detecting millilensing effects in at least one of the two macroimages of a source depends on both M_{IMBH} and F_{IMBH}. However, this value is considered to be $P_{\mathrm{IMBH}} \sim 1$ in all IMBH cases explored (For detailed explanation see section 5.2).

Examples of simulation results in both HR and LR cases for IMBHs are presented in figures 5.7 & 5.8. Even though F_{IMBH} varies for different M_{IMBH}, the number density variations follow the mass difference, i.e. by increasing M_{IMBH} from 10^3 to $10^6 M_{\odot}$, the number density drops from $\sim 10^{-2}$ to $\sim 10^{-5}\mathrm{pc}^{-1}$. This is due to the fact that all assumed F_{IMBH}s are at the same order of magnitude. However, since the sizes of simulation regions vary for each M_{IMBH} due to detectability considerations, the number of subhalos inside the simulation region does not follow this pattern.

Moreover, the distortions in the two macroimages are not correlated in any way, therefore the millilensing effects are distinguishable from intrinsic jet features which appear in both macroimages similarly. Hence, as it is clear in figures corresponding to $M_{\mathrm{IMBH}} = 10^4$, 10^5, and $10^6 M_{\odot}$, millilensing effects of these substructures are clearly detectable. On the other hand, the distortions made by $10^3 M_{\odot}$ IMBHs would be distinguishable from the noise only

in observations with very good sensitivity.

Furthermore, the value of the CDM fraction in the form of IMBHs where we expect all explored cases to be affected by the presence of a single IMBH in the simulation region $F^{\rm PN}_{\rm IMBH}$ for different simulated observational modes are shown in table 5.8. The mass-dependence of this parameter for IMBHs compared to UCMHs and NFWs is presented in figure 5.13.

Overall, although the effect of decreasing resolution in constraining the detectable mass range is predictable, the change due to resolution drop from LR (22 GHz observations) to VLR (8.4 GHz observations) is very prominent. As indicated in table 5.8, although the source size in the VLR case is 100 times that of the LR, the smallest detectable substructure mass decreases by a factor of 100, merely by a 3-folded decrease in the resolution.

Frequency (GHz)	Mass ($M_\odot$)	$F^{\rm PN}_{\rm IMBH}$
86	10^3	2×10^{-1}
86	10^4	9×10^{-2}
86	10^5	1×10^{-1}
86	10^6	2×10^{-1}
22	10^4	3×10^{-1}
22	10^5	1×10^{-1}
22	10^6	2×10^{-1}
8.4	10^5	7×10^{-2}
8.4	10^6	2×10^{-2}

Table 5.8: The lowest halo mass fraction in IMBHs, $F_{\rm IMBH}$, that would produce detectable millilensing distortions with $P_{\rm IMBH} \simeq 100\%$ probability in a single macroimage pair.

5.5.2 Detecting UCMHs

As expected through comparing the density profiles, UCMHs are not as efficient in lensing as IMBHs are. This is partly manifested in the mass range of the UCMHs for which sub-milliarcsecond distortions are in principle detectable in the observations we consider. As the mass ranges in table 5.9 indicate, the less-massive UCMHs giving rise to image distortions in both HR and LR cases are as massive as the most massive IMBHs assumed, $10^6 M_\odot$. This comparison shows an even more prominent difference for UCMHs with the larger source size and poorer resolution, i.e. the VLR case; UCMH lower mass limit in this case is $10^8 M_\odot$.

Besides, our simulations show that even in the most optimistic cases of having all the main halo mass in the form of UCMHs, $F_{\rm UCMH} \sim 1$, the probability of detecting small-scale distortion in at least one of the macroimages of a jet is approximately 100 times smaller than

that of IMBHs with the same mass. This is immediately clear in $F^{\rm PN}_{\rm UCMH}$ values in table 5.9 which mostly are of the order of 100 (recall that we fixed this value to 1 for IMBHs).

Similar to the case of IMBHs, samples of how a UCMH in the simulation region affects the two macroimages of a small source (jet size 4×1 pc) are presented in figures 5.9 and 5.10 for the HR and LR simulated observations, respectively.

The Einstein radii of UCMHs with $M_{\rm UCMH} = 10^6 M_\odot$ are so small that unless the millilens is projected close to the brightest parts of the macroimage, it would hardly be distinguishable from noise in the radio map. Besides, although the Einstein radii of single UCMHs increase considerably with mass, the detection probabilities of HR observations remain at a same level while increasing the mass from 10^6 to $10^{10} M_\odot$. The same result applies to the LR and VLR cases as well (see figure 5.13).

Accordingly, UCMHs are not promising substructures to be detectable through gravitational millilensing effects given the resolution options and source sizes we consider.

Table 5.9: The lowest halo mass fraction in UCMHs, $F_{\rm UCMH}$, that would produce detectable millilensing distortions with $P_{\rm UCMH} \simeq 100\%$ probability in a single macroimage pair.

Frequency (GHz)	Mass ($M_\odot$)	$F^{\rm PN}_{\rm UCMH}$
86	10^6	1.1×10^2
86	10^7	9.9×10^1
86	10^8	9.1×10^1
86	10^9	6.0×10^1
86	10^{10}	2.6×10^2
22	10^6	9.1×10^2
22	10^7	2.3×10^2
22	10^8	1.9×10^2
22	10^9	8.3×10^1
22	10^{10}	2.6×10^2
8.4	10^8	2.0×10^1
8.4	10^9	7.9×10^0
8.4	10^{10}	4.4×10^0

5.5.3 Detecting NFWs

NFWs, assumed to represent standard CDM halos, are principally not detectable through the type/scale of effects we have studied throughout this work. Table 5.10 shows the mass contribution to the CDM mass of the parent halo required from NFWs to produce detectable

millilensing effects in almost all observed images. Recalling that $F_{\rm NFW}^{\rm PN}$ is defined as dark matter *fraction*, the immediate conclusion from table 5.10 is that NFWs cannot be probed by this method in this scale. This conclusion applies to all resolutions and jet sizes, since all the entries in this column are of the order 10^3.

Moreover, in our MC samplings to adopt the desired mass function to these substructures, only subhalos with $M_{\rm NFW} \leq 10^7 M_\odot$ are numerous enough to attain a decent probability of showing up in the simulation region. According to the results indicated in table 5.3 and figure 5.11, such low mass NFWs do not produce detectable distortions, even to be detected through the HR mode. (The same result obtained for both $F_{\rm NFW} = 0.02$ and $F_{\rm NFW} = 0.002$)

In figures 5.11and 5.12, we show examples of the most severe effects produced by NFW subhalos in different mass bins. It is clear from the images that $10^7 M_\odot$ NFWs only produce distortions in the source morphology which would be detectable through high-sensitivity observations of HR, where the multiple images due to 10^8 and $10^9 M_\odot$s are expected to be detected at least in the HR case. However, we have to keep in mind that these images are produced by placing NFWs close to the macroimage, which would happen very rarely (see figure 5.14).

Frequency (GHz)	Mass ($M_\odot$)	$F_{\rm NFW}^{\rm PN}$
86	10^7	1.8×10^3
86	10^8	1.1×10^3
86	10^9	4.7×10^2
22	10^7	5.4×10^3
22	10^8	2.3×10^3
22	10^9	4.7×10^2
8.4	10^8	2.2×10^3
8.4	10^9	9.9×10^3

Table 5.10: The lowest halo mass fraction in NFWs, $F_{\rm NFW}$, that would produce detectable millilensing distortions with $P_{\rm NFW} \simeq 100\%$ probability in a single macroimage pair.

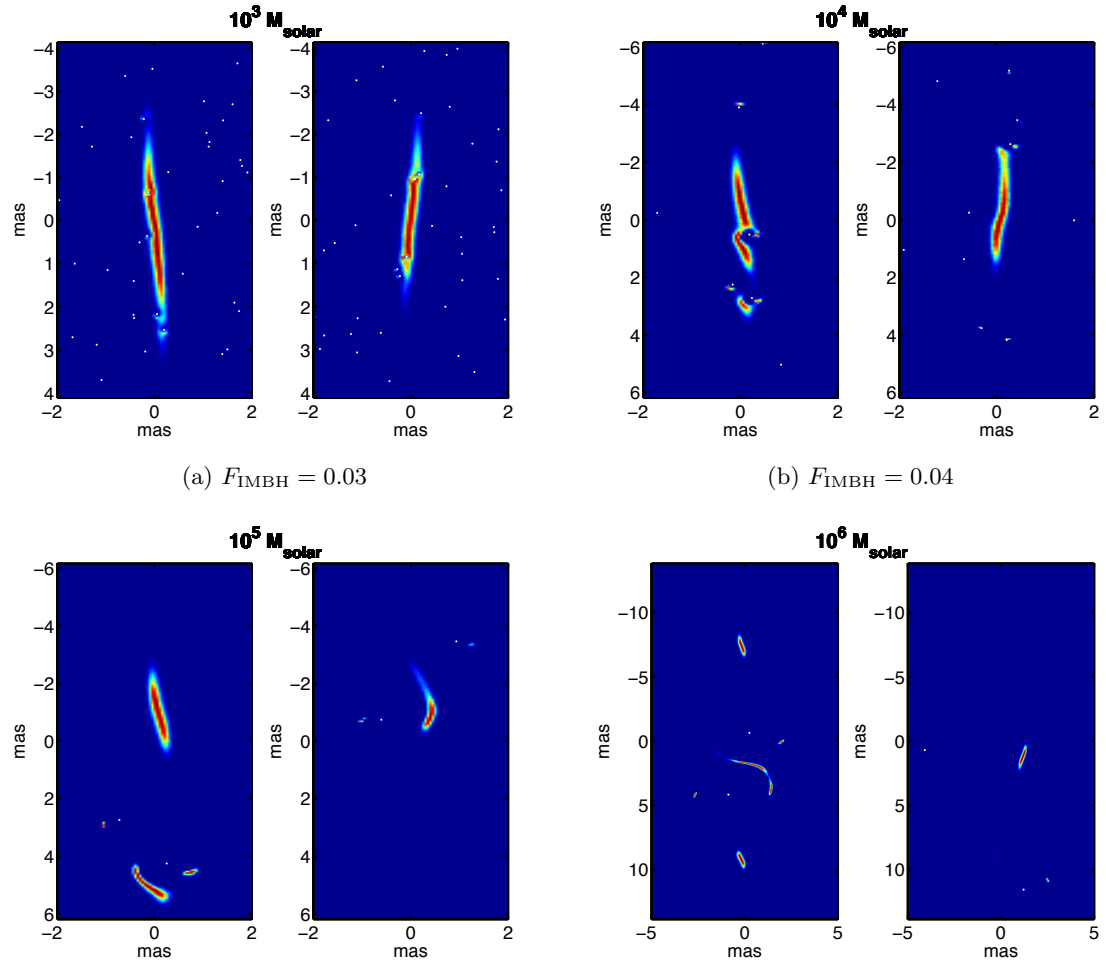

(a) $F_{\mathrm{IMBH}} = 0.03$

(b) $F_{\mathrm{IMBH}} = 0.04$

(c) $F_{\mathrm{IMBH}} = 0.06$

(d) $F_{\mathrm{IMBH}} = 0.1$

Figure 5.7: Simulated radio maps of a strongly lensed quasar jet in the HR case (intrinsic source size 4×1 pc) subject to millilensing distortions due to IMBHs with various F_{IMBH}s as mentioned below each image. Each image pair shows two macroimages produced by the main lens (the parent halo). The positions of the IMBHs are indicated by white dots. Notice that the scales differ from mass to mass.

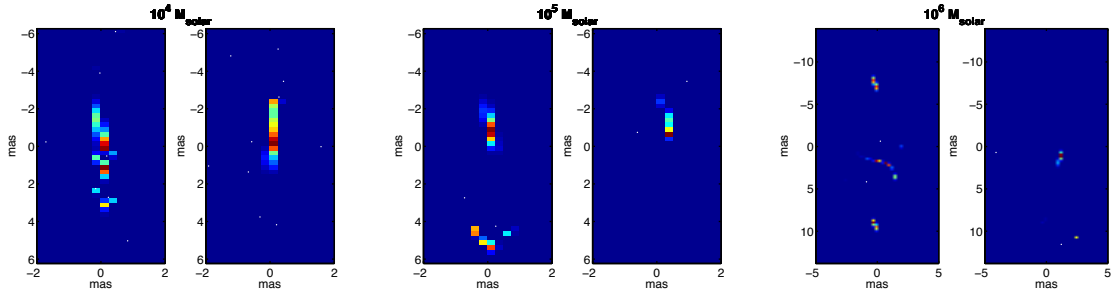

(a) $F_{\rm IMBH} = 0.04$ (b) $F_{\rm IMBH} = 0.06$ (c) $F_{\rm IMBH} = 0.1$

Figure 5.8: Simulated radio maps of a strongly lensed quasar jet at LR case (intrinsic source size 4×1 pc) subject to millilensing distortions due to IMBHs with various $F_{\rm IMBH}$s as mentioned below each image. Each image pair shows two macroimages produced by the main lens (the parent halo). The positions of the IMBHs are indicated by white dots. Notice that the scales differ from mass to mass

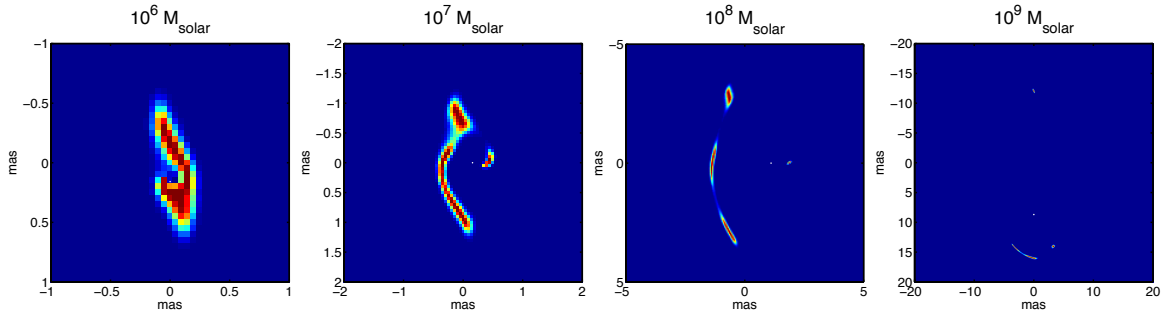

Figure 5.9: Simulated radio maps of a strongly lensed quasar jet in the HR case (intrinsic source size 4×1 pc) subject to millilensing distortions due to UCMHs with $F_{\rm UCMH} \sim 1$. The positions os the UCMHs are indicated by white dots. Notice that the scales differ from mass to mass.

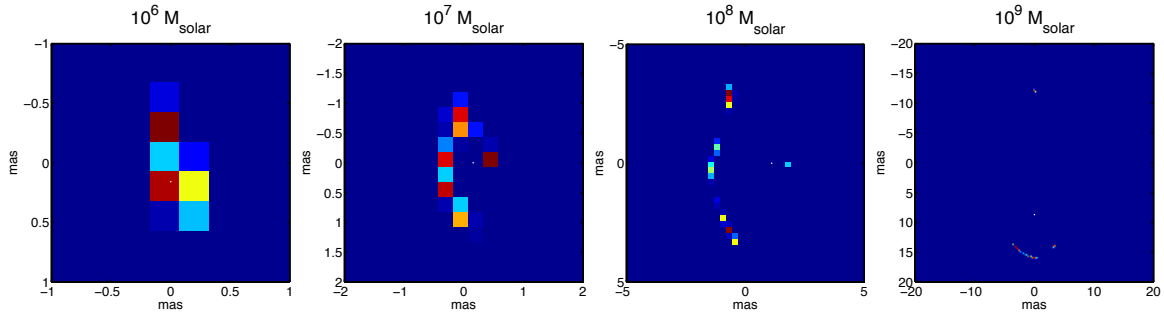

Figure 5.10: Simulated radio maps of a strongly lensed quasar jet in the LR case (intrinsic source size 4×1 pc) subject to millilensing distortions due to UCMHs with $F_{\mathrm{UCMH}} \sim 1$. The positions os the UCMHs are indicated by white dots. Notice that the scales differ from mass to mass.

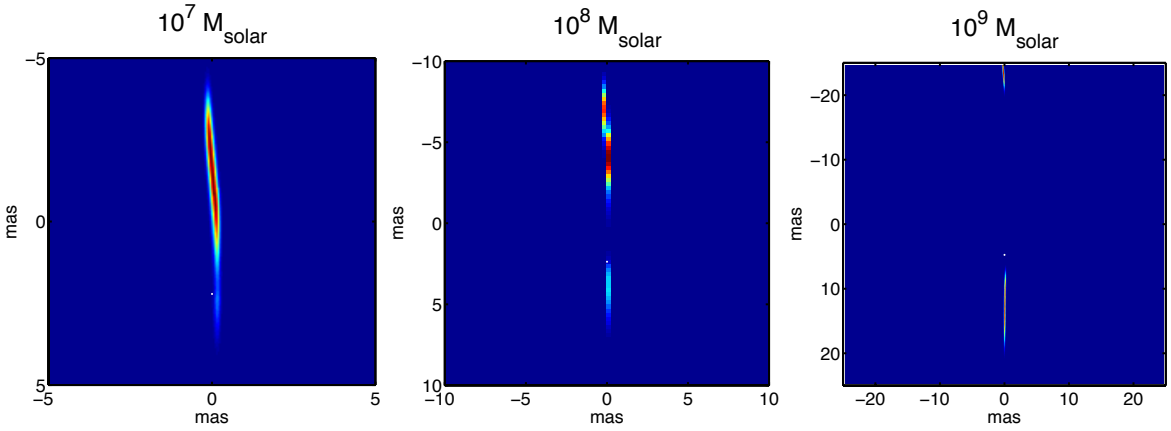

Figure 5.11: Simulated radio maps of a strongly lensed quasar jet in the HR case (intrinsic source size 4×1 pc) subject to millilensing distortions due to NFWs with $F_{\mathrm{NFW}} = 0.02$. The positions os the NFWs are indicated by white dots. Notice that the scales differ from mass to mass.

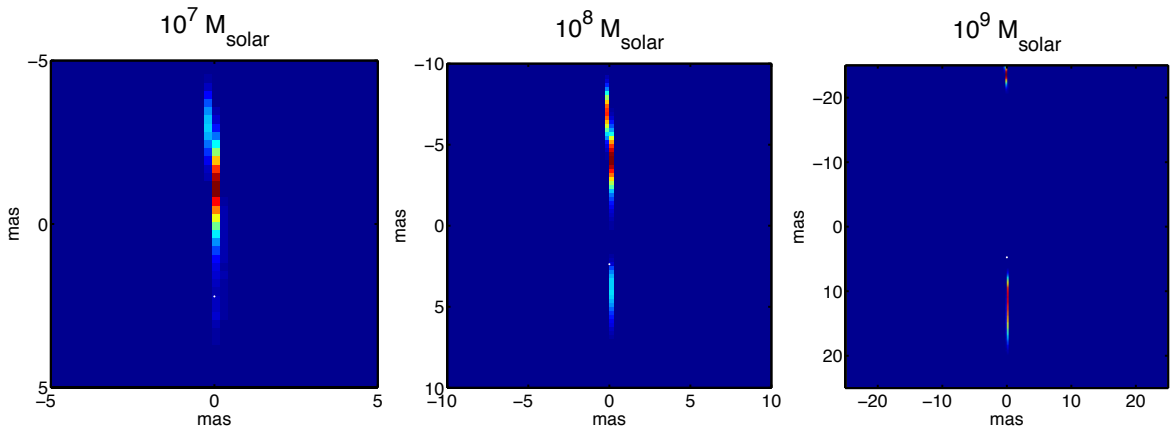

Figure 5.12: Simulated radio maps of a strongly lensed quasar jet in the LR case (intrinsic source size 4×1 pc) subject to millilensing distortions due to NFWs with $F_{\mathrm{NFW}} = 0.02$. The positions os the NFWs are indicated by white dots. Notice that the scales differ from mass to mass.

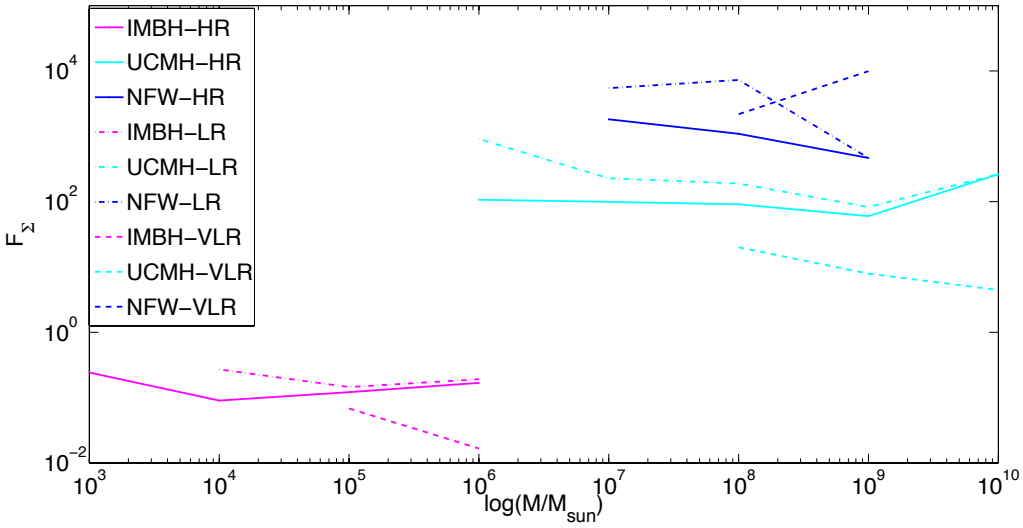

Figure 5.13: The substructure mass contribution with respect to the CDM halo mass required to achieve detectability of roughly 100 % with the assumed resolutions and source sizes, F_Σ^{PN}s. Magenta lines represent IMBHs, cyans denote UCMHs and dark blue lines indicate NFWs in different simulation modes; solid lines: HR mode (jet size 4×1 pc, resolution 0.05 mas, observed in 86 GHz), dashed-dotted lines: LR mode (jet size 4×1 pc, resolution 0.25 mas, observed in 22 GHz), and dashed lines: VLR mode (jet size 40×10 pc, resolution 0.7 mas, observed in 8.4 GHz). The only substructure type showing $F_\Sigma^{\mathrm{PN}} < 1$, so principally detectable, is IMBH in all resolutions.

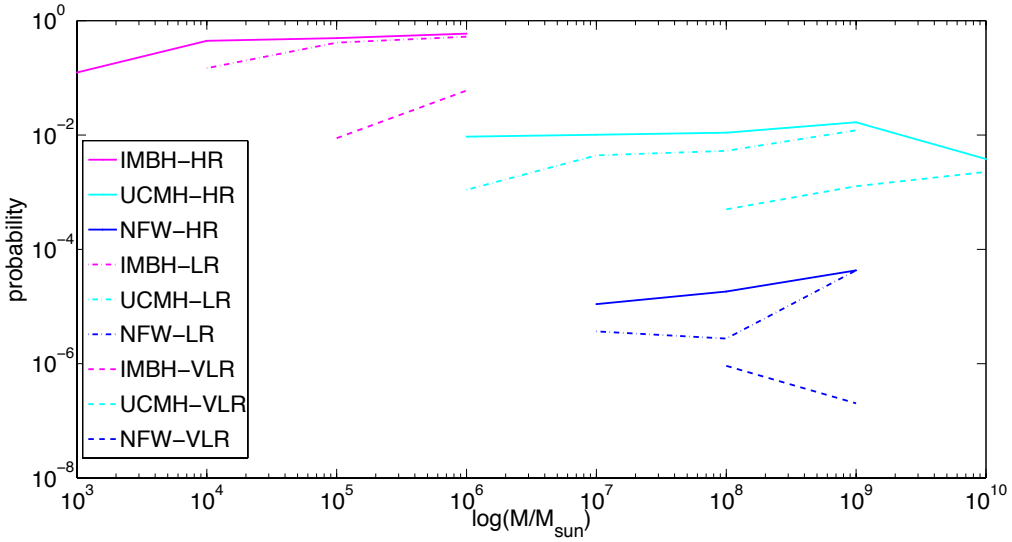

Figure 5.14: The probabilities of detecting millilensing effects in various types of substructure. As pointed out in the text, IMBHs in different mass bins have different $F_{\rm IMBH}$ values. However, $F_{\rm UCMH}$ is set to $\simeq 1$, i.e. the most optimistic situation, for all masses. On the other hand, the DM mass fraction for NFWs, $F_{\rm NFW} = 0.02$, is assumed. Even in such optimistic cases, several hundred/thousand (millions) observations are required to detect sub-milliarcsecond-scale image distortions produced by UCMHs (NFWs).

CHAPTER 6

Discussion

In previous chapters we discussed small-scale morphological distortions produced by dark halo substructures. We can only distinguish such image distortions from intrinsic features by observing both macroimages of a source produced by the main lens. The distortions which do not show up in both images are referred to as millilensing effects due to substructures here. However, there might be other reasons giving rise to such distortions. The time delay between lensed image pairs of a source can be up to a year (Oguri, 2007). On the other hand, the effective source-plane velocity of the lens system (as estimated by Kochanek (2004) this value is of the order 10^4 km/s) gives rise to a miliarcsecond-scale position change in substructure configurations at redshift 2 within a period of ~ 1000 years. In this regard, unless the image pair is observed for over a year we cannot ascribe the small-scale distortions appearing in one macroimage to halo substructures.

Besides, we assume all substructures to be in the lens plane which is not necessarily the case. The light ray could be subject to more than a single halo-subhalo system. Line-of-sight contamination with substructures can in principle happen at any redshift between the main lens and the observer. Such effect could give rise to an unrealistic subhalo model if the redshift-dependence of the millilens is not considered properly. This degeneracy is not easily broken, but on the other hand unless the abundance of detected millilenses is peculiarly high, it would not strongly affect the results such as ours.

Furthermore, according to our results presented in the previous chapter and the already proven substructure detections by Vegetti et al. (2010, 2012) using the HST, even if observed

with lower resolutions, larger sources seem to be more probable targets to reveal dark halo substructures. In our case, the larger source is roughly 100 times of the smaller one and is assumed to be observed by a resolution ~ 3 (14) times worse, however, the final detection probabilities are ~ 10 times worse than both HR and LR cases. Moreover, the detected substructures by Vegetti et al. (2010, 2012), are observed by studying image distortions on almost complete Einstein rings using angular resolutions of 2-3 orders of magnitude lower than our resolutions. On the other hand, such cases (large source, poor angular resolution) is biased to massive substructures, as it is clear from our results in chapter 5 and in previously mentioned observations which found substructures as massive as $\sim 10^9 M_\odot$ (Vegetti et al., 2010) and $\sim 10^8 M_\odot$ (Vegetti et al., 2012) as suitable subhalo models to reproduce the observed image distortions.

Summary

The majority of the mass contain of the universe has long been believed to be in “dark mater”, which we usually are not able to observe directly through its radiation. On the other hand, one of the long-known phenomena related to massive objects is how a light ray passing through a gravitational field is bent. This phenomenon, later called gravitational lensing, was fully described using the theory of general relativity and was confirmed in the beginning of the twentieth century. Gravitational lensing became one of the promising tools to study the existence and properties of dark matter structures in the universe.

Among the debatable theories of the dark matter, the cold dark matter (CDM) model is generally accepted at the current time. However, this model has not yet been successful in predicting the consistent cosmological abundance of low-mass CDM halos with the observed abundance of faint dwarf galaxies. This discrepancy is persistent in the case of detected dwarf satellites around the Milky Way and Andromeda and the dark subhalos in the corresponding mass range. The long-standing issue is commonly referred to as “the missing satellites problem”.

The present thesis includes the results obtained from a set of computer simulations modeling present or upcoming radio arrays with submilliarcsecond angular resolutions. The target is a pc-sized radio-loud quasar which is strongly lensed into multiple images due to the presence of a galaxy-sized dark halo and each macroimage is subject to millilensing image distortions due to dark halo substructures within the host halo. Three density profiles and masses are examined for the dark substructures; including the standard dark halo substructures, Navarro-Frenk-White (NFW) subhalos; and the two alternative candidates which may give rise to such small-scale effects; intermediate-mass black holes (IMBHs) and the ultracom-

pact minihalos (UCMHs). The latter candidates are not among the resulting density profiles from the CDM model, however they are thought to have a substantial contribution to the dark matter according to some astronomers. If so, according to our result, the observations with near future instruments will be able to confirm their existence. The standard CDM dark halo profiles on the other hand, are not efficient lenses within the simulated resolutions and unless the source size is peculiarly large, they do not show detectable millilensing effects.

There have recently been observations (Vegetti et al., 2010, 2012) showing anomalies in Einstein rings of sources with the Hubble Space Telescope (HST) which show consistent results as CDM-based simulations. These observations support the results from this study that millilensing effects due to dark halo substructures are detectable even with lower resolutions as long as the target is strongly magnified into large macroimages due to the host galaxy.

Bibliography

Begelman M. C., Volonteri M., Rees M. J., 2006, MNRAS, 370, 289

Bode P., Ostriker J. P., Turok N., 2001, ApJ, 556, 93

Bradač M., Schneider P., Steinmetz M., Lombardi M., King L. J., Porcas R., 2002, A&A, 388, 373

Bringmann T., Huang X., Ibarra A., Vogl S., Weniger C., 2012, ArXiv e-prints

Bringmann T., Scott P., Akrami Y., 2011, ArXiv e-prints

Buckley M. R., Hooper D., 2010, PhRvD, 82, 063501

Bullock J. S., Kolatt T. S., Sigad Y., Somerville R. S., Kravtsov A. V., Klypin A. A., Primack J. R., Dekel A., 2001, MNRAS, 321, 559

Carr B. J., Kohri K., Sendouda Y., Yokoyama J., 2010, PhRvD, 81, 104019

Chen J., Koushiappas S. M., Zentner A. R., 2011, ApJ, 741, 117

Colombi S., Dodelson S., Widrow L. M., 1996, ApJ, 458, 1

Dalal N., Kochanek C. S., 2002, ApJ, 572, 25

Davies M. B., Miller M. C., Bellovary J. M., 2011, APJL, 740, L42

Davis M., Efstathiou G., Frenk C. S., White S. D. M., 1985, ApJ, 292, 371

Devecchi B., Volonteri M., 2009, ApJ, 694, 302

Dyson F. W., Eddington A. S., Davidson C., 1920, Royal Society of London Philosophical Transactions Series A, 220, 291

Gao L., Frenk C. S., Boylan-Kolchin M., Jenkins A., Springel V., White S. D. M., 2011, MNRAS, 410, 2309

Hooper D., Kaplinghat M., Strigari L. E., Zurek K. M., 2007, PhRvD, 76, 103515

Kauffmann G., White S. D. M., Guiderdoni B., 1993, MNRAS, 264, 201

Keeton C. R., 2001, ApJ, 561, 46

Klypin A., Kravtsov A. V., Valenzuela O., Prada F., 1999, ApJ, 522, 82

Kochanek C. S., 2004, ApJ, 605, 58

Komatsu E. et al., 2009, APJS, 180, 330

Komatsu E. et al., 2011, APJS, 192, 18

Macciò A. V., Dutton A. A., van den Bosch F. C., 2008, MNRAS, 391, 1940

Maciejewski M., Vogelsberger M., White S. D. M., Springel V., 2011, MNRAS, 415, 2475

Metcalf R. B., Madau P., 2001, ApJ, 563, 9

Metcalf R. B., Zhao H., 2002, ApJ, 567, L5

Moore B., Ghigna S., Governato F., Lake G., Quinn T., Stadel J., Tozzi P., 1999, APJL, 524, L19

Moustakas L. A. et al., 2009, in ArXiv Astrophysics e-prints, Vol. 2010, astro2010: The Astronomy and Astrophysics Decadal Survey, p. 214

Narayan R., Bartelmann M., 1996, ArXiv Astrophysics e-prints

Navarro J. F., Frenk C. S., White S. D. M., 1996, ApJ, 462, 563

Oguri M., 2007, ApJ, 660, 1

Refsdal S., 1964, MNRAS, 128, 307

Ricotti M., Gould A., 2009, ApJ, 707, 979

Ricotti M., Ostriker J. P., Mack K. J., 2008, ApJ, 680, 829

Riehm T., Zackrisson E., Mörtsell E., Wiik K., 2009, ApJ, 700, 1552

Scott P., Sivertsson S., 2009, Physical Review Letters, 103, 211301

Spergel D. N. et al., 2007, APJS, 170, 377

Spergel D. N., Steinhardt P. J., 2000, Physical Review Letters, 84, 3760

Springel V. et al., 2008, MNRAS, 391, 1685

Torniainen I. et al., 2008, AAP, 482, 483

Totani T., 2010, PASJ, 62, L1

Treu T., 2010, ARA&A, 48, 87

Vegetti S., Koopmans L. V. E., Bolton A., Treu T., Gavazzi R., 2010, MNRAS, 408, 1969

Vegetti S., Lagattuta D. J., McKean J. P., Auger M. W., Fassnacht C. D., Koopmans L. V. E., 2012, Nature, 481, 341

Walsh D., Carswell R. F., Weymann R. J., 1979, Nature, 279, 381

White S. D. M., Rees M. J., 1978, MNRAS, 183, 341

Xu D. D., Mao S., Cooper A. P., Wang J., Gao L., Frenk C. S., Springel V., 2010, MNRAS, 408, 1721

Yonehara A., Umemura M., Susa H., 2003, PASJ, 55, 1059

Zackrisson E., Riehm T., 2010, Advances in Astronomy, 2010

Zackrisson E., Riehm T., Möller O., Wiik K., Nurmi P., 2008, ApJ, 684, 804

Zwicky F., 1933, Helvetica Physica Acta, 6, 110

Zwicky F., 1937, Physical Review, 51, 290